J. Fluid Mech. (2005), *vol.* 526, *pp.* 77–115.
DOI: 10.1017/S0022112004002678 Printed in the United Kingdom

Curvature instability of a vortex ring

By YASUHIDE FUKUMOTO[1] AND YUJI HATTORI[2]

[1]Graduate School of Mathematics and Space Environment Research Center, Kyushu University 33, Fukuoka 812-8581, Japan

[2]Faculty of Engineering, Kyushu Institute of Technology, Kitakyushu 804-8550, Japan

(Received 19 January 2004 and in revised form 16 July 2004)

A global stability analysis of Kelvin's vortex ring to three-dimensional disturbances of infinitesimal amplitude is made. The basic state is a steady asymptotic solution of the Euler equations, in powers of the ratio ϵ of the core radius to the ring radius, for an axisymmetric vortex ring with vorticity proportional to the distance from the symmetric axis. The effect of ring curvature appears at first order, in the form of a dipole field, and a local straining field, which is a quadrupole field, follows at second order. The eigenvalue problem of the Euler equations, retaining the terms to first order, is solved in closed form, in terms of the Bessel and the modified Bessel functions. We show that the dipole field causes a parametric resonance instability between a pair of Kelvin waves whose azimuthal wavenumbers are separated by 1. The most unstable mode occurs in the short-wavelength limit, under the constraint that the radial and the azimuthal wavenumbers are of the same magnitude, and the limiting value of maximum growth rate coincides with the value $165/256\epsilon$ obtained by Hattori & Fukumoto (*Phys. Fluids*, vol. 15, 2003, p. 3151) by means of the geometric optics method. The instability mechanism is traced to stretching of disturbance vorticity in the toroidal direction. In the absence of viscosity, the dipole effect outweighs the straining field effect of $O(\epsilon^2)$ known as the Moore–Saffman–Tsai–Widnall instability. The viscosity acts to damp the former preferentially and these effects compete with each other.

1. Introduction

Vortex rings are invariably susceptible to wavy distortions, leading sometimes to violent wiggles and eventually to disruption (Maxworthy 1972, 1977; Widnall & Sullivan 1973). It has been found that the Moore–Saffman–Tsai–Widnall instability, abbreviated as the MSTW instability, is responsible for the genesis of the unstable waves (Widnall, Bliss & Tsai 1974; Moore & Saffman 1975; Tsai & Widnall 1976; Widnall & Tsai 1977; Shariff & Leonard 1992). Note that this is an instability for a straight vortex tube subjected to a straining field in a plane perpendicular to the tube axis.

When viewed locally, a thin vortex ring looks like a straight tube. For simplicity, we restrict our attention to the Rankine vortex, a circular core of uniform vorticity. Because of circular-cylindrical symmetry, the Rankine vortex is neutrally stable and supports a family of three-dimensional waves of infinitesimal amplitude, known as Kelvin waves. The vortex ring induces, on itself, not only a local uniform flow that drives a translational motion as a whole, but also a local straining field akin to a pure shear, in the meridional plane, with principal axes tilted by $\pi/4$ from the symmetric axis (Widnall *et al.* 1974). This is a quadrupole field proportional to $\cos 2\theta$ and $\sin 2\theta$, in terms of local polar coordinates (r, θ) in the meridional plane, with its origin at the

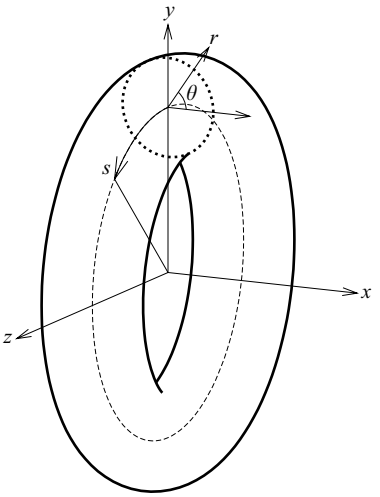

FIGURE 1. Toroidal coordinates (r, θ, s) comoving with the ring. The origin $r = 0$ in the meridional plane coincides with the centre of the core. s is the arclength parameter along the centre circle.

core centre and with $\theta = 0$ along the travelling direction (see figure 1). This field breaks the circular symmetry of the core by deforming it into an ellipse, and feeds parametric resonance between two Kelvin waves whose azimuthal wavenumbers are separated by 2 (Gledzer *et al.* 1975; Moore & Saffman 1975; Tsai & Widnall 1976; Gledzer & Ponomarev 1992; Eloy & Le Dizès 2001; Fukumoto 2003). In the short-wavelength regime, the MSTW instability becomes the elliptical instability found by Bayly (1986) (see also Waleffe 1990; Leweke & Williamson 1998), implying the ubiquity of the MSTW instability (Kerswell 2002); the influence of neighbouring vortices is, in the leading-order approximation, incorporated as a linear shear flow.

However this picture might be too crude to fit a curved vortex tube. The asymptotic solution of the Navier–Stokes or the Euler equations for a thin vortex ring in powers of a small parameter ϵ, the ratio of the core to the ring radii, starts with a circular-cylindrical vortex tube at $O(\epsilon^0)$. A vortex ring is characterized by curvature of vortex lines. This feature manifests itself, at $O(\epsilon^1)$, as a local dipole field proportional to $\cos\theta$ and $\sin\theta$. The quadrupole field comes merely as a correction at $O(\epsilon^2)$ (Dyson 1893; Fraenkel 1972; Fukumoto & Moffatt 2000; Fukumoto 2002). Despite its dominance, the dipole field has not attracted as much attention as it deserves. This may be because, in a typical situation of planar flows, the local dipole field is trivially associated with the degree of freedom of coordinate translation. But in three dimensions, it is an essential ingredient for vortex-line curvature. This paper addresses a possible instability when the dipole field comes into play.

According to Krein's theory of parametric resonance in Hamiltonian systems (MacKay 1986), a single Kelvin wave cannot be fed by perturbations breaking the circular symmetry. An instability becomes possible only for superposition of at least two modes with the same wavenumber and the same frequency. Subjected to the dipole field, two Kelvin waves with angular dependence $e^{im\theta}$ and $e^{in\theta}$ can be amplified cooperatively at the intersection points of dispersion curves if the condition $|m - n| = 1$ is met.

The linear stability analysis was fully formulated by Widnall & Tsai (1977, hereinafter referred to as WT77), but the dipole effect has not been studied. Fukumoto & Hattori (2002) verified that a combination of the axisymmetric ($m = 0$) and the bending

($n=1$) waves indeed leads to parametric resonance. The local stability analysis of Hattori & Fukumoto (2003), based on the geometric optics method devised by Lifschitz & Hameiri (1991), disclosed the existence of more unstable resonance via the dipole field.

These results stimulate us to examine all possible resonant azimuthal-wavenumber pairs $(m, m+1)$ of Kelvin waves. It will be shown that the most dangerous instability mode takes place in the limit of $m \to \infty$. Unlike the instability of quadrupole-field origin, not all multiple eigenvalues result in resonance. The necessary condition for instability, brought out by Krein's theory, is either that the eigenvalue collision occurs between a positive- and a negative-energy mode or that the collision eigenvalue is zero. The energy of Kelvin waves, which was calculated by Fukumoto (2003), is instrumental in making a distinction between resonant and non-resonant eigenvalue collisions.

In § 2, we give a concise description of the problem setting for a linear stability analysis. We allow for small viscosity and the Navier–Stokes equations to be handled are written down in Appendix A. The Kelvin waves are recalled in Appendix B. Section 3 seeks the solution of the linearized Navier–Stokes equations. Remarkably, Kelvin's vortex ring admits a closed-form solution, in terms only of the Bessel and the modified Bessel functions, for the disturbance velocity field, and so do the growth rate and the width of the unstable wavenumber band. Computer algebra is indispensable in deriving the solution, and the detailed form of the solution is relegated to Appendix C. Section 4 is concerned with the inviscid resonance instability. We present numerical examples of growth rate, band width and unstable velocity field for some choices of azimuthal wavenumber pairs. The explicit solution is amenable to an asymptotic analysis, and the short-wave asymptotics is dealt with in § 5, supplemented by Appendix D. A comparison with the local stability analysis, made by Hattori & Fukumoto (2003), reveals the passage from global to local instability. The asymptotic form of the eigenfunction shows that stretching of the toroidal vorticity of the disturbance field is the source for instability. In § 6, the present instability at $O(\epsilon)$ is compared with that at $O(\epsilon^2)$ with viscosity taken into consideration. Section 7 is devoted to a summary and conclusions.

2. Setting of linear stability problem

The global linear stability analysis in three dimensions was formulated by WT77. We employ their notation. As an extension, we make an attempt to treat weak viscous dissipation in parallel with the treatment of Eloy & Le Dizès (2001).

Kelvin's vortex ring is a thin axisymmetric vortex ring, in an incompressible inviscid fluid, with vorticity proportional to the distance from the axis of symmetry. It propagates steadily in the direction of the axis of symmetry with translation speed given by

$$\frac{\Gamma}{4\pi R}\left\{\log\left(\frac{8R}{\sigma}\right)-\frac{1}{4}\right\}, \tag{2.1}$$

where Γ is the circulation carried by the ring, σ is the core radius and R is the ring radius. Our assumption is that the radius ratio ϵ is very small:

$$\epsilon = \sigma/R \ll 1. \tag{2.2}$$

An expression for the flow field outside the core was written out in full to $O(\epsilon^4)$ by Dyson (1893). The flow field both inside and around the core can be found in WT77 and Fukumoto (2002). In reality, it is the interior flow field that is indispensable for our purpose.

We introduce toroidal coordinates (r, θ, s) comoving with the ring as shown by figure 1. In the meridional plane $s = 0$, the origin $r = 0$ is maintained at the centre of the circular core and the angle θ is measured from the direction parallel to the axis of symmetry, the x-axis say, and thus (r, θ) may be thought of as local polar coordinates. The centre circle penetrating the toroidal ring is parameterized by the arclength s. The global Cartesian coordinates (x, y, z) are then expressed by

$$x = r\cos\theta, \quad y = (R + r\sin\theta)\cos(s/R), \quad z = (R + r\sin\theta)\sin(s/R). \tag{2.3}$$

We normalize the radial coordinate r by the core radius σ, the velocity by the maximum azimuthal velocity $\Gamma/2\pi\sigma$, the time t by $2\pi\sigma^2/\Gamma$ and the pressure by $\rho_f(\Gamma/2\pi\sigma)^2$ with ρ_f being the density of fluid. Let the r and θ components of the velocity field be U and V, respectively, and the pressure be P inside the core ($r < 1$). The velocity potential for the exterior irrotational flow is denoted by Φ. Appendix A contains the Navier–Stokes equations expressed in the toroidal coordinates.

The basic flow is expanded in powers of ϵ, the first-order truncation of which takes the form

$$\left.\begin{aligned} &U = \epsilon U_1(r,\theta) + \cdots, \quad V = V_0(r) + \epsilon V_1(r,\theta) + \cdots, \\ &P = P_0(r) + \epsilon P_1(r,\theta) + \cdots \quad \text{for } r < 1, \end{aligned}\right\} \tag{2.4}$$

$$\Phi = \Phi_0(\theta) + \epsilon\Phi_1(r,\theta) + \cdots \quad \text{for } r > 1. \tag{2.5}$$

The leading-order flow is the Rankine vortex as expressed, in dimensionless form, by

$$V_0 = r, \quad P_0 = \tfrac{1}{2}(r^2 - 1), \quad \Phi_0 = \theta. \tag{2.6}$$

The first-order flow field is a dipole field:

$$\left.\begin{aligned} &U_1 = \tfrac{5}{8}(1 - r^2)\cos\theta, \quad V_1 = \left(-\tfrac{5}{8} + \tfrac{7}{8}r^2\right)\sin\theta, \quad P_1 = \left(-\tfrac{5}{8}r + \tfrac{3}{8}r^3\right)\sin\theta, \\ &\Phi_1 = \left(\tfrac{1}{8}r - \frac{3}{8r} - \tfrac{1}{2}r\log r\right)\cos\theta. \end{aligned}\right\} \tag{2.7}$$

To this order, the circular form of the core boundary ($r = 1$) remains intact.

The velocity field for $r > 1$ is

$$U_1 = -\tfrac{3}{8}\left(1 - \frac{1}{r^2} + \tfrac{4}{3}\log r\right)\cos\theta, \quad V_1 = -\tfrac{1}{8}\left(1 - \frac{3}{r^2} - 4\log r\right)\sin\theta. \tag{2.8}$$

Disregarding the terms with $\log r$, (2.8) is equivalent to the flow past a circular cylinder of unit radius with uniform velocity $-3\epsilon/8$ in the x-direction at infinity. More appropriately, this may be interpreted as a flow induced by a vortex pair of curvature origin. Vortex lines of a steady vortex ring are stretched on the convex side and are contracted on the concave side of the torus. As a result, the vorticity is enhanced on the convex side and is weakened on the concave side, producing effectively a vortex pair (Fukumoto 2002).

We examine the evolution of three-dimensional disturbances of infinitesimal amplitude superposed on the above steady flow. Following the prescription of Moore & Saffman (1975) and Tsai & Widnall (1976), we expand the disturbance velocity $\tilde{\boldsymbol{v}}$, the disturbance pressure $\tilde{p}$ and the external disturbance velocity potential $\tilde{\phi}$ in powers of ϵ to first order:

$$\left.\begin{aligned} &\tilde{\boldsymbol{v}} = \mathrm{Re}\left[(\boldsymbol{v}_0 + \epsilon\boldsymbol{v}_1 + \cdots)\mathrm{e}^{\mathrm{i}(ks-\omega t)}\right], \quad \tilde{p} = \mathrm{Re}\left[(\pi_0 + \epsilon\pi_1 + \cdots)\mathrm{e}^{\mathrm{i}(ks-\omega t)}\right], \\ &\tilde{\phi} = \mathrm{Re}\left[(\phi_0 + \epsilon\phi_1 + \cdots)\mathrm{e}^{\mathrm{i}(ks-\omega t)}\right], \end{aligned}\right\} \tag{2.9}$$

where the symbol Re designates the real part. In keeping with this form, the wavenumber k and the frequency ω, non-dimensionalized by $1/\sigma$ and $\Gamma/(2\pi\sigma^2)$ respectively, are also expanded as

$$k = k_0 + \epsilon k_1 + \cdots, \quad \omega = \omega_0 + \epsilon\omega_1 + \cdots. \tag{2.10}$$

The disturbed edge of the core is expanded as

$$r = 1 + \tilde{f}_0(\theta, s, t) + \epsilon\tilde{f}_1(\theta, s, t) + \cdots. \tag{2.11}$$

3. Effect of the dipole field

The flow field $\boldsymbol{v}_0$, π_0 and ϕ_0 and the dispersion relation $\omega_0 = \omega_0(k_0)$ of Kelvin waves are contained in Appendix B (see, for example, Kopiev & Chernyshev 1997; Kop'ev & Chernyshev 2000). Our concern is the modification of Kelvin's dispersion relation due to the symmetry-breaking action of the $O(\epsilon)$ dipole field.

3.1. *Linearized equations*

We assume that the viscosity ν is so small that the circulation Reynolds number R_Γ is at least of $O(\epsilon^{-1})$:

$$R_\Gamma = \frac{\Gamma}{\nu} \gtrsim O(\epsilon^{-1}). \tag{3.1}$$

The toroidal component of the disturbance velocity is designated by w. Equations governing the amplitude vector $\boldsymbol{v}_1$ of the disturbance velocity and the amplitude π_1 of the disturbance pressure of $O(\epsilon)$, inside the core ($r < 1$), are derived from the Navier–Stokes equations written in toroidal coordinates (r, θ, s), in Appendix A, as

$$\begin{aligned}
-\mathrm{i}\omega_0 u_1 + \frac{\partial u_1}{\partial\theta} - 2v_1 + \frac{\partial\pi_1}{\partial r} &= \left(\mathrm{i}\omega_1 - \frac{\partial U_1}{\partial r}\right)u_0 - U_1\frac{\partial u_0}{\partial r} - \frac{V_1}{r}\frac{\partial u_0}{\partial\theta} \\
&\quad - \left(\frac{1}{r}\frac{\partial U_1}{\partial\theta} - \frac{2V_1}{r}\right)v_0 + \tilde{\nu}\left\{\left(\frac{\partial^2}{\partial r^2} + \frac{1}{r}\frac{\partial}{\partial r} + \frac{1}{r^2}\frac{\partial^2}{\partial\theta^2} - k_0^2 - \frac{1}{r^2}\right)u_0 - \frac{2}{r^2}\frac{\partial v_0}{\partial\theta}\right\}, \qquad (3.2)\\
-\mathrm{i}\omega_0 v_1 + 2u_1 + \frac{\partial v_1}{\partial\theta} + \frac{1}{r}\frac{\partial\pi_1}{\partial\theta} &= \left(\mathrm{i}\omega_1 - \frac{1}{r}\frac{\partial V_1}{\partial\theta} - \frac{U_1}{r}\right)v_0 - \left(\frac{\partial V_1}{\partial r} + \frac{V_1}{r}\right)u_0 \\
&\quad - U_1\frac{\partial v_0}{\partial r} - \frac{V_1}{r}\frac{\partial v_0}{\partial\theta} + \tilde{\nu}\left\{\left(\frac{\partial^2}{\partial r^2} + \frac{1}{r}\frac{\partial}{\partial r} + \frac{1}{r^2}\frac{\partial^2}{\partial\theta^2} - k_0^2 - \frac{1}{r^2}\right)v_0 + \frac{2}{r^2}\frac{\partial u_0}{\partial\theta}\right\}, \qquad (3.3)\\
-\mathrm{i}\omega_0 w_1 + \frac{\partial w_1}{\partial\theta} + \mathrm{i}k_0\pi_1 &= -\mathrm{i}k_1\pi_0 + (\mathrm{i}\omega_1 - r\cos\theta)w_0 - \frac{V_1}{r}\frac{\partial w_0}{\partial\theta} - U_1\frac{\partial w_0}{\partial r} \\
&\quad + \mathrm{i}k_0 r\pi_0\sin\theta + \tilde{\nu}\left(\frac{\partial^2}{\partial r^2} + \frac{1}{r}\frac{\partial}{\partial r} + \frac{1}{r^2}\frac{\partial^2}{\partial\theta^2} - k_0^2\right)w_0, \qquad (3.4)
\end{aligned}$$

where the normalized viscosity $\tilde{\nu}$ of $O(\epsilon^0)$ is

$$\tilde{\nu} = \frac{2\pi\nu}{\Gamma\epsilon} = \frac{2\pi}{R_\Gamma\epsilon}. \tag{3.5}$$

The equation of continuity is

$$\frac{\partial u_1}{\partial r} + \frac{u_1}{r} + \frac{1}{r}\frac{\partial v_1}{\partial\theta} + \mathrm{i}k_0 w_1 = -u_0\sin\theta - v_0\cos\theta + \mathrm{i}k_0 r w_0\sin\theta. \tag{3.6}$$

The amplitude function ϕ_1 of the velocity potential for the disturbance flow of $O(\epsilon)$, outside the core ($r > 1$), satisfies

$$\frac{\partial^2\phi_1}{\partial r^2} + \frac{1}{r}\frac{\partial\phi_1}{\partial r} + \frac{1}{r^2}\frac{\partial^2\phi_1}{\partial r^2} - k_0^2\phi_1 = 2k_0k_1\phi_0 - \sin\theta\frac{\partial\phi_0}{\partial r} - \frac{\cos\theta}{r}\frac{\partial\phi_0}{\partial\theta} - 2k_0^2 r\phi_0\sin\theta. \quad (3.7)$$

The boundary conditions require that the normal component of the velocity and the pressure be continuous across the interface ($r = 1$) of the core:

$$\left.\begin{aligned} u_1 &= \frac{\partial\phi_1}{\partial r}, \\ \pi_1 - \mathrm{i}\omega_0\phi_1 + \frac{\partial\phi_1}{\partial\theta} &= \mathrm{i}\omega_1\phi_0 - \frac{\partial\Phi_1}{\partial\theta}\frac{\partial\phi_0}{\partial\theta}. \end{aligned}\right\} \quad (3.8)$$

The shape of disturbed core boundary is found from

$$\mathrm{i}\omega_0 f_1 - \frac{\partial f_1}{\partial\theta} + u_1 = -\mathrm{i}\omega_1 f_0 + V_1\frac{\partial f_0}{\partial\theta} - \frac{\partial U_1}{\partial r}f_0. \quad (3.9)$$

The right-hand sides of (3.2)–(3.9) include the coupling of Kelvin waves with the dipole field (2.7) of $O(\epsilon)$. Note that (3.2)–(3.4), (3.6) and (3.7) correspond to (7.1*a*–*e*) of WT77, augmented with viscous terms, and that (3.8) and (3.9) correspond to (7.2) of WT77. We follow WT77's formulation, generalized to higher azimuthal-wavenumber resonance.

Suppose that a pair of Kelvin waves whose azimuthal wavenumbers differ by 1 are simultaneously put at $O(\epsilon^0)$:

$$\boldsymbol{v}_0 = \boldsymbol{v}_0^{(1)}\mathrm{e}^{\mathrm{i}m\theta} + \boldsymbol{v}_0^{(2)}\mathrm{e}^{\mathrm{i}(m+1)\theta}. \quad (3.10)$$

Here and hereafter, we use superscripts (1) and (2) for the m and the $m+1$ waves respectively. In view of the dipole field on the right-hand sides of (3.2)–(3.7) and the boundary conditions (3.8), the wave excited at $O(\epsilon)$ is found to possess the following angular dependence:

$$\boldsymbol{v}_1 = \boldsymbol{v}_1^{(1)}\mathrm{e}^{\mathrm{i}m\theta} + \boldsymbol{v}_1^{(2)}\mathrm{e}^{\mathrm{i}(m+1)\theta} + \boldsymbol{v}_1^{(3)}\mathrm{e}^{\mathrm{i}(m-1)\theta} + \boldsymbol{v}_1^{(4)}\mathrm{e}^{\mathrm{i}(m+2)\theta}. \quad (3.11)$$

A similar form is given to π_0, ϕ_0 and π_1, ϕ_1. Excitation, at $O(\epsilon)$, of a pair of waves with the same azimuthal wavenumbers as at $O(\epsilon^0)$ implies a possibility of parametric resonance.

The leading-order disturbance is, from Appendix A,

$$\left.\begin{aligned} \phi_0 &= K_m(k_0r)\alpha_0^{(1)}\mathrm{e}^{\mathrm{i}m\theta} + K_{m+1}(k_0r)\alpha_0^{(2)}\mathrm{e}^{\mathrm{i}(m+1)\theta}, \\ \pi_0 &= J_m(\eta_1r)\beta_0^{(1)}\mathrm{e}^{\mathrm{i}m\theta} + J_{m+1}(\eta_2r)\beta_0^{(2)}\mathrm{e}^{\mathrm{i}(m+1)\theta}, \end{aligned}\right\} \quad (3.12)$$

where J_m and K_m are, respectively, the Bessel function of the first kind and the modified Bessel function of the second kind, m being their order, $\alpha_0^{(1)}$, $\alpha_0^{(2)}$, $\beta_0^{(1)}$ and $\beta_0^{(2)}$ are constants, and η_1 and η_2 are the radial wavenumbers of the m and the $m+1$ waves respectively as defined by (B 4) and (B 8). Likewise, the interior velocity field (u_0, v_0, w_0) is expressible as superposition of expressions (B 3) for the m and $m+1$ waves.

Upon substituting from (3.12), (3.7) becomes

$$\mathrm{M}^{(1)}\left[\phi_1^{(1)}\right] = 2k_0k_1K_m(k_0r)\alpha_0^{(1)} + \mathrm{i}k_0\left\{\tfrac{1}{2}K_m(k_0r) - k_0rK_{m+1}(k_0r)\right\}\alpha_0^{(2)}, \quad (3.13)$$

$$\mathrm{M}^{(2)}\left[\phi_1^{(2)}\right] = 2k_0k_1K_{m+1}(k_0r)\alpha_0^{(2)} + \mathrm{i}k_0\left\{k_0rK_m(k_0r) - \tfrac{1}{2}K_{m+1}(k_0r)\right\}\alpha_0^{(1)}, \quad (3.14)$$

where

$$\mathrm{M}^{(i)} = \frac{\mathrm{d}^2}{\mathrm{d}r^2} + \frac{1}{r}\frac{\mathrm{d}}{\mathrm{d}r} - \left(\frac{m_i^2}{r^2} + k_0^2\right) \quad (i = 1, 2), \quad (3.15)$$

with $m_1 = m$ and $m_2 = m+1$. A general solution of (3.13) and (3.14), finite at infinity, is found to be

$$\phi_1^{(1)} = K_m(k_0 r)\alpha_1^{(1)} - k_1 r K_{m+1}(k_0 r)\alpha_0^{(1)} + \frac{\mathrm{i}}{4}\{k_0 r^2 K_m(k_0 r) + (2m+1) r K_{m+1}(k_0 r)\}\alpha_0^{(2)}, \quad (3.16)$$

$$\phi_1^{(2)} = K_{m+1}(k_0 r)\alpha_1^{(2)} - k_1 r K_m(k_0 r)\alpha_0^{(2)} + \frac{\mathrm{i}}{4}\{(2m+1) r K_m(k_0 r) - k_0 r^2 K_{m+1}(k_0 r)\}\alpha_0^{(1)}, \quad (3.17)$$

where $\alpha_1^{(1)}$ and $\alpha_1^{(2)}$ are constants added to the homogeneous parts of the solution.

For the vortical disturbance in the core, (3.2)–(3.6) constitute a coupled system of ordinary equations for the amplitude functions of r. An efficient method for numerical integration of the eigenvalue problem is to adapt, to the ring geometry, the inner-product formulation of Moore & Saffman (1975) which was originally derived for an elliptically strained vortex tube. Its details are left out.

Analytical handling becomes feasible, to a large extent, by collapsing (3.2)–(3.6), at the outset, to second-order ordinary differential equations for the disturbance pressure $\pi_1^{(1)}$ and $\pi_1^{(2)}$. After some computer algebra, we are left with

$$\mathrm{L}^{(1)}[\pi_1^{(1)}] = \left\{\frac{8k_0^2\omega_1}{(\omega_0-m)^3} - \frac{2k_1}{k_0}\eta_1^2\right\} J_m(\eta_1 r)\beta_0^{(1)} - \mathrm{i}\left\{\left[\frac{1}{2} + \frac{3m}{2(\omega_0-m-1)} - \frac{5k_0^2}{4}\left(\frac{1}{(\omega_0-m)^2} - \frac{1}{(\omega_0-m-1)^2}\right)(r^2-1)\right]\eta_2 J_m(\eta_2 r) + \left[1 + \frac{8\omega_0-9m-1}{2(\omega_0-m)^2} - \frac{7\omega_0-9m-19}{4(\omega_0-m-1)^2}\right]k_0^2 r J_{m+1}(\eta_2 r)\right\}\beta_0^{(2)} + \frac{32\mathrm{i}\tilde{\nu}k_0^4}{(\omega_0-m)^5} J_m(\eta_1 r)\beta_0^{(1)}, \quad (3.18)$$

$$\mathrm{L}^{(2)}[\pi_1^{(2)}] = \left\{\frac{8k_0^2\omega_1}{(\omega_0-m-1)^3} - \frac{2k_1}{k_0}\eta_2^2\right\} J_{m+1}(\eta_2 r)\beta_0^{(2)} + \frac{\mathrm{i}}{4}\left\{\left[4 + \frac{7\omega_0-9m+10}{(\omega_0-m)^2} - \frac{2(8\omega_0-9m-8)}{(\omega_0-m-1)^2}\right]k_0^2 r J_m(\eta_2 r) - \left[2 + \frac{6(m+1)}{\omega_0-m-2} + 5k_0^2\left(\frac{1}{(\omega_0-m)^2} - \frac{1}{(\omega_0-m-1)^2}\right)(r^2-1)\right]\eta_1 J_{m+1}(\eta_1 r)\right\}\beta_0^{(1)} + \frac{32\mathrm{i}\tilde{\nu}k_0^4}{(\omega_0-m-1)^5} J_{m+1}(\eta_2 r)\beta_0^{(2)}, \quad (3.19)$$

where η_1 and η_2 are defined by (B 4) and (B 8) respectively, and

$$\mathrm{L}^{(i)} = \frac{\mathrm{d}^2}{\mathrm{d}r^2} + \frac{1}{r}\frac{\mathrm{d}}{\mathrm{d}r} - \frac{m_i^2}{r^2} + \eta_i^2 \quad (i = 1, 2). \quad (3.20)$$

The boundary conditions (3.8) are, for the m wave,

$$u_1^{(1)} - \frac{\partial\phi_1^{(1)}}{\partial r} = 0, \quad \pi_1^{(1)} - \mathrm{i}(\omega_0-m)\phi_1^{(1)} = \mathrm{i}\omega_1\phi_0^{(1)} + \frac{m+1}{8}\phi_0^{(2)}, \quad (3.21)$$

and, for the $m+1$ wave,

$$u_1^{(2)} - \frac{\partial\phi_1^{(2)}}{\partial r} = 0, \quad \pi_1^{(2)} - \mathrm{i}(\omega_0-m-1)\phi_1^{(2)} = \mathrm{i}\omega_1\phi_0^{(2)} - \frac{m}{8}\phi_0^{(1)}. \quad (3.22)$$

3.2. *Disturbance field and growth rate*

WT77 omitted the solution for $\boldsymbol{v}_1$. We are now ready to construct the solution of (3.18) and (3.19) and to calculate the $O(\epsilon)$ correction ω_1 to the eigenfrequency from the boundary conditions (3.21) and (3.22).

By appealing to symbolic calculus, the solution of (3.18) and (3.19) is obtained in closed form solely in terms of the Bessel functions. The resulting expressions for $\pi_1^{(1)}$, $\pi_1^{(2)}$, $u_1^{(1)}$ and $u_1^{(2)}$, the enforcement of the boundary conditions (3.21) and (3.22) and the solvability conditions on them are written down in Appendix C.

We recapitulate the procedure of Moore & Saffman (1975) and Tsai & Widnall (1976). For the moment, we leave out the viscosity. Simultaneous excitation of at least two Kelvin waves is requisite for instability, being indicative of parametric resonance. The postulation that the solvability conditions (C 11) and (C 12) have a non-trivial solution of $\beta_0^{(1)} \neq 0$ and $\beta_0^{(2)} \neq 0$ gives rise to ω_1. Instability is implied when $\mathrm{Im}[\omega_1] > 0$ and we write its growth rate as $\sigma_1 = |\mathrm{Im}[\omega_1]|$. In the case of instability, the growth rate takes its local maximum value $\sigma_{1\max}$ at $k = k_0$, namely $k_1 = 0$, and $\mathrm{Im}[\omega_1] > 0$ only over a limited wavenumber range of width $2\epsilon\Delta k_1$ centred on $k = k_0$. The desired formulae for $\sigma_{1\max}$ and Δk_1 are obtained from (C 11) and (C 12) as

$$\sigma_{1\max}^2 = -\frac{(\omega_0-m)^3(\omega_0-m-1)^3(\omega_0-m+1)(\omega_0-m+2)(\omega_0-m-2)(\omega_0-m-3)}{1024k_0^4(2\omega_0-2m-1)^4} \times \frac{h^2}{f^{(1)}f^{(2)}}, \quad (3.23)$$

$$\Delta k_1^2 = -\frac{(\omega_0-m)^3(\omega_0-m-1)^3(\omega_0-m+1)(\omega_0-m+2)(\omega_0-m-2)(\omega_0-m-3)}{1024k_0^2(2\omega_0-2m-1)^4} \times \frac{f^{(1)}f^{(2)}h^2}{d^2}, \quad (3.24)$$

where

$$d = (\omega_0-m)(\omega_0-m+2)(\omega_0-m-2)f^{(2)}g^{(1)} - (\omega_0-m-1)(\omega_0-m+1)(\omega_0-m-3)f^{(1)}g^{(2)}, \quad (3.25)$$

and the form of $f^{(1)}$, $f^{(2)}$, $g^{(1)}$, $g^{(2)}$ and h is given in (C 13)–(C 17).

4. Examples of inviscid resonance

To give an illustration, we carry out a numerical computation of the stability characteristics for two cases. We begin with a resonance mode of the simplest azimuthal structure.

4.1. *Resonance between the* 0, 1 *waves*

The dispersion relation of Kelvin waves of $m = 0$ (dashed lines) and $m = 1$ (solid lines) is displayed in figure 2. The isolated branch of $m = 1$, starting from $\omega_0 = 0$, is drawn with a thick solid line. Infinitely many branches emanate from $(k_0, \omega_0) = (0, 1)$ for $m = 1$ among which forty branches, twenty upward and twenty downward, are drawn. These modes are named the radial modes since the eigenfunctions have non-trivial radial nodal structure. A wave with $|\omega_0| > 1$ rotates faster than the basic circulatory flow and is called a cograde mode, which is distinguished from a wave with $|\omega_0| < 1$, a retrograde mode (Saffman 1992). In contrast, an isolated branch and the counterpart of the retrograde modes are missing for the axisymmetric mode. Given the wavenumber k_0, the modes with ω_0 and $-\omega_0$ share a common property of a cograde radial mode.

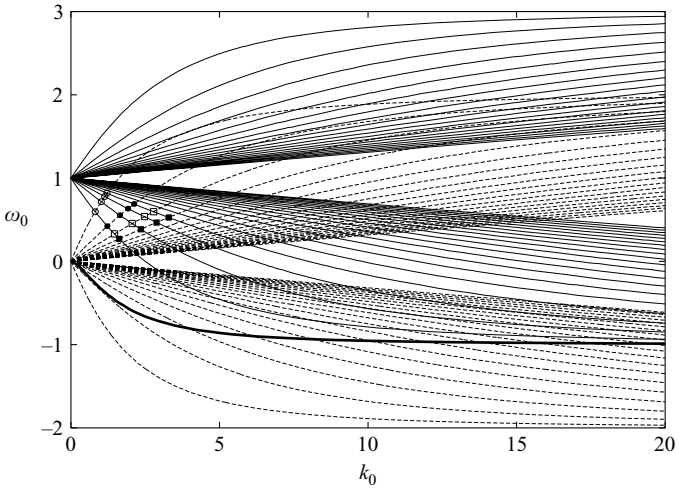

FIGURE 2. Dispersion relation of the axisymmetric wave $m=0$ (dashed lines) and the helical wave $m=1$ (solid lines) on the Rankine vortex. The isolated branch of $m=1$ is shown with a thick line. The symbols are discussed in the text.

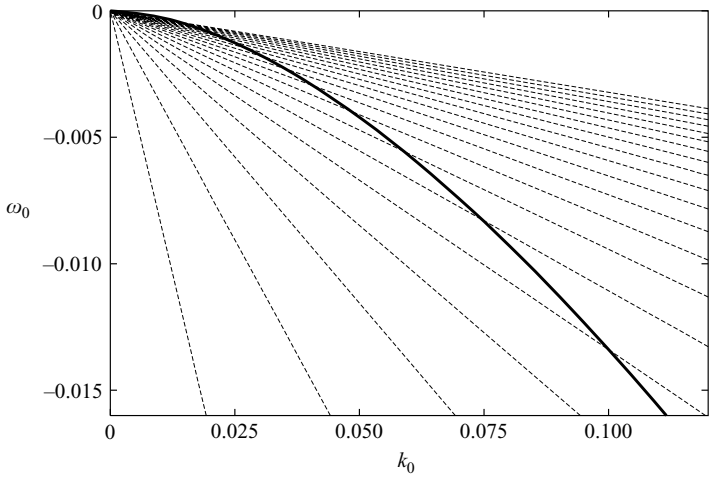

FIGURE 3. Close-up view of figure 2 near $(k_0, \omega_0) = (0, 0)$.

A positive axisymmetric mode ($\omega_0 > 0$) crosses every retrograde mode of $m=1$ once, and may cross some of higher cograde branches of $m=1$ twice. A negative axisymmetric mode ($\omega_0 < 0$) collides, if its branch index is high enough, with some of the retrograde radial modes of $m=1$, twice for each. The isolated mode of $m=1$ crosses branches of $m=0$ at small values of k_0 as is seen from the close-up view in figure 3 of near the origin of figure 2.

The growth rate (3.23) is calculated at many of intersection points. A collision of eigenvalues of the 0, 1 waves does not necessarily result in instability. Stability is lost only at intersection points between positive branches of $m=0$ and retrograde radial modes of $m=1$, and not otherwise. This behaviour is in stark contrast with that of the MSTW instability. In the latter case, every eigenvalue collision potentially involves parametric resonance (Eloy & Le Dizès 2001; Fukumoto 2003). The energetics holds the key to distinguishing non-resonant collisions from resonant ones, as will be described in §4.3.

k_0	ω_0	$\sigma_{1\max}$	Δk_1
0.8134868347	0.5970895378	0.05434123370	0.1022075453
1.018687659	0.7162537484	0.007063858086	0.01725321243
1.136862167	0.7794574187	0.008676095366	0.02449637577
1.214999401	0.8191926924	0.007511646111	0.02329133797
1.224505620	0.4217998862	0.03931853915	0.1093080415
1.650449151	0.5528357882	0.03769686682	0.1381880078
1.927505750	0.6329096309	0.004366456551	0.01889368333
2.126154076	0.6877694566	0.007048839587	0.03418778188
1.464572874	0.3290672352	0.02466638188	0.08406115354
2.059092345	0.4537065585	0.01547299060	0.07032354299
2.472533079	0.5364030938	0.03273541819	0.1773468081
2.783117712	0.5962177954	0.002632427093	0.01613293863
1.625453596	0.2707234248	0.01708461632	0.06631547378
2.351745150	0.3860821416	0.01652875697	0.08656816266
2.879959092	0.4669749326	0.004710163249	0.02962775154
3.289680122	0.5277784143	0.03038502117	0.2175329321

TABLE 1. The maximum growth rate $\epsilon\sigma_{1\max}$ and the half-width $\epsilon\Delta k_1$ of the unstable wavenumber band to $O(\epsilon)$ for the (0,1) resonance. See text for details.

In table 1, we list the evaluated values of the growth rate and the unstable bandwidth for low wavenumbers. The first four rows correspond to the first four intersection points of the first positive axisymmetric mode ($m=0$) with retrograde radial modes of $m=1$, marked with open circles in figure 2. The next four rows are along the second mode of $m=0$ (solid circles), and then along the third mode of $m=0$ (open squares) and the last four are along the fourth mode (solid squares). Since the torus centre is a circle of radius R, an unstable mode is realizable only when the arclength $2\pi R$ coincides with some integral multiple of the wavelength $2\pi/k_0$. The unstable bandwidth needs to be sufficiently broad.

A large growth rate is maintained to short wavelengths at intersection points between the ith branch of $m=0$ and the ith branch of the retrograde radial modes of $m=1$. This sequence belongs to what we call the principal modes. Apparently, the growth rate is relatively large at intersection points along the first retrograde mode of $m=1$, but this mode decreases as the branch number i is increased. The half-width Δk_1 is large at intersection points of large growth rate.

The origin $(k_0, \omega_0)=(0, 0)$ is the intersection point between the isolated branch of $m=1$ and all branches of $m=0$. For a general $(m, m+1)$ resonance, (3.23) and (3.24) tend, as $k_0\to 0$ and $\omega_0\to m$, to

$$\sigma_{1\max}^2=\frac{(m+1)(3m+2)^2(\omega_0-m)^5}{32k_0^4}, \tag{4.1}$$

$$\Delta k_1^2=\frac{(m+1)(3m+2)^2(\omega_0-m)^3}{8(2m+3)^2k_0^2}. \tag{4.2}$$

From the dispersion relation of Kelvin waves at small values of k_0 (Kopiev & Chernyshev 1997; Fukumoto 2003), the frequency is at least $\omega_0=m+O(k_0)$ as $k_0\to 0$, and therefore the limit of (4.1) and (4.2) as $k_0\to 0$ should be taken as $\sigma_{1\max}=0$ and $\Delta k_1=0$. For the 0, 1-pair, the origin is a neutrally stable point. Incidentally, following Crow (1970), calculation of the Biot-Savart law for vortex-ring stability to bending

waves of long wavelengths was undertaken by Widnall & Sullivan (1973). Their instability mode was found to be spurious by Widnall *et al.* (1974), in accord with the result, in the localized induction approximation, of Arms & Hama (1965) that a circular-line vortex is neutrally stable.

Among the intersection points examined so far, the maximum of growth rate is attained at the first principal mode, namely at $(k_0, \omega_0) \approx (0.8134868347, 0.5970895378)$, though the maximum value $\sigma_{1\max} \approx 0.05434123370$ is not very large. The corresponding flow field is calculated, to $O(\epsilon^0)$, from (3.10) with $\boldsymbol{v}_0^{(1)}$ and $\boldsymbol{v}_0^{(2)}$ provided in Appendix B. The solvability conditions (C 9) and (C 10) give $\beta_0^{(2)}/\beta_0^{(1)} \approx 0.7276318666$ at this point. With this value, the shape of the core boundary is drawn in perspective view in figure 4. It is observed that the fore–aft symmetry is broken with larger deformation on the front side. Flow visualization reflects pressure field. Figure 5 depicts contours of pressure on longitudinal planes $\theta = \text{const.}$ through the centre of a rectified torus, and figure 6 depicts the same on several meridional planes $s = \text{const.}$ To fix the origin of the phase, we put $t = 0$. The line of local pressure minimum draws a helix winding around the toroidal centre, with fore–aft symmetry broken.

The contours of toroidal velocity w_0 on the cross-sectional plane $k_0 s = \omega_0 t$ are drawn in figure 7. Only the interior region ($r < 1$) is shown. A strong toroidal or axial current is induced over a very large region with the location of peak velocity pushed backward from the core centre, and is accompanied by a small counter-current in the front part of the core. The location of peak velocity winds helically around the torus centre, and executes a circulatory motion around the centre. Figure 8(*a*) displays the disturbance vorticity field $(\omega_{0r}, \omega_{0\theta})$ of $O(\epsilon^0)$ projected on the same cross-sectional plane. The contours of toroidal vorticity ω_{0s} are shown in figure 8(*b*). The ring-like vorticity structure in figure 8(*a*) corresponds to the strong toroidal flow in figure 7. The toroidal vorticity is large at points where the toroidal current is weak.

We reason that, as with the cases of the elliptical instability (Waleffe 1990) and of the instability due to multi-polar strain (Eloy & Le Dizès 2001), the instability mechanism is attributable to parallelization between the stretching direction of local shear and the disturbance vorticity. The strain tensor due to the first-order field (2.7) of the base flow is

$$\epsilon r \begin{pmatrix} -\frac{5}{4}\cos\theta & \frac{3}{4}\sin\theta & 0 \\ \frac{3}{4}\sin\theta & \frac{1}{4}\cos\theta & 0 \\ 0 & 0 & \cos\theta \end{pmatrix} = \epsilon \begin{pmatrix} -\frac{5}{4}x & \frac{3}{4}y & 0 \\ \frac{3}{4}y & \frac{1}{4}x & 0 \\ 0 & 0 & x \end{pmatrix}. \tag{4.3}$$

Here local Cartesian coordinates $(x, y, s) = (r\cos\theta, r\sin\theta, s)$ have been introduced with some abuse of notation. The eigenvalues and their associated eigenvectors are

$$\lambda_1 = \epsilon r \left(-\frac{\cos\theta}{2} + \frac{3}{4} \right), \quad \boldsymbol{e}_1 = \begin{pmatrix} \sin\frac{1}{2}\theta \\ \cos\frac{1}{2}\theta \\ 0 \end{pmatrix}, \tag{4.4a}$$

$$\lambda_2 = \epsilon r \left(-\frac{\cos\theta}{2} - \frac{3}{4} \right), \quad \boldsymbol{e}_2 = \begin{pmatrix} \cos\frac{1}{2}\theta \\ -\sin\frac{1}{2}\theta \\ 0 \end{pmatrix}, \tag{4.4b}$$

$$\lambda_3 = \epsilon r \cos\theta, \quad \boldsymbol{e}_3 = \begin{pmatrix} 0 \\ 0 \\ 1 \end{pmatrix}. \tag{4.4c}$$

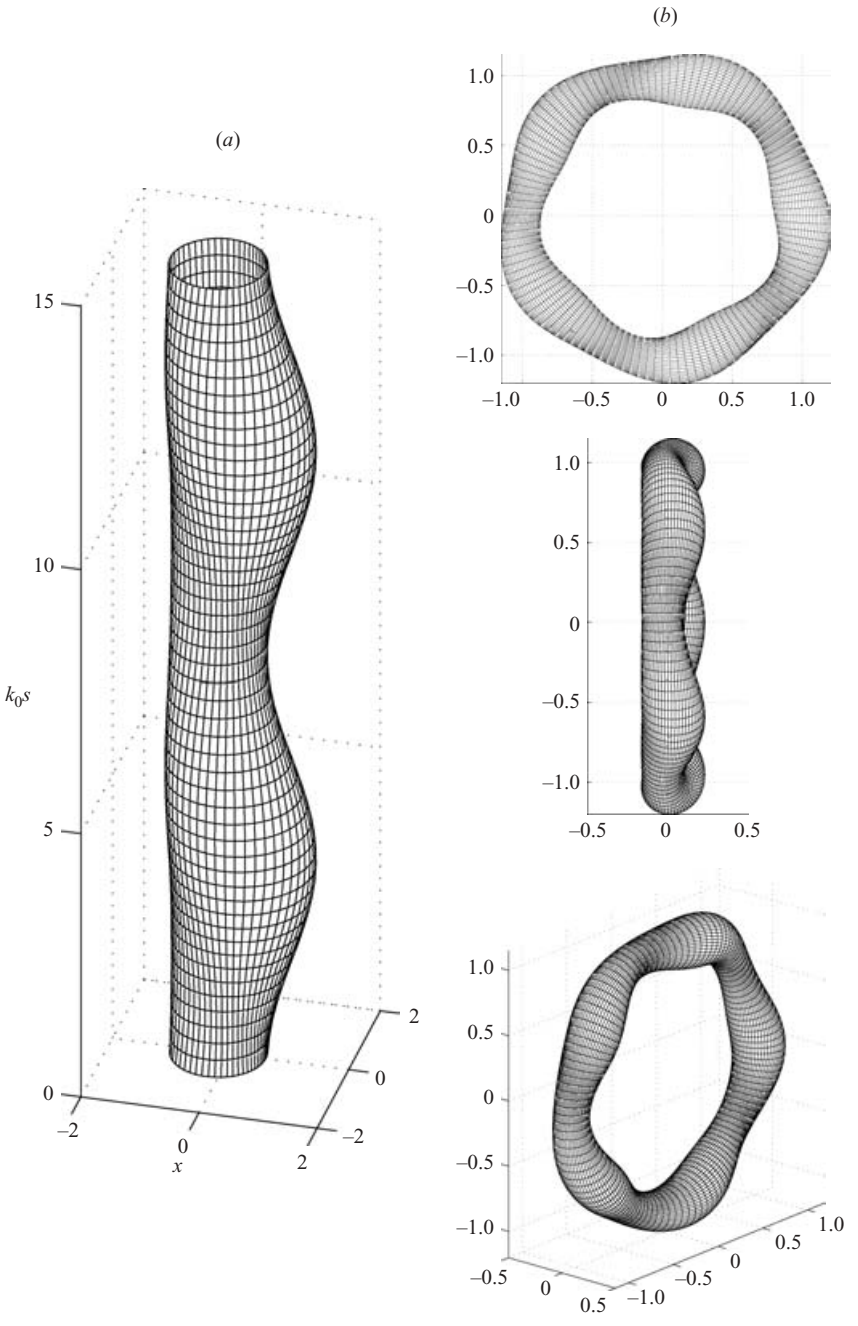

FIGURE 4. Shape of the disturbed vortex ring for the first principal mode of the (0, 1) resonance excited at $(k_0, \omega_0) \approx (0.8134868347, 0.5970895378)$. (*a*) $\epsilon = 0$, (*b*) $\epsilon = 0.1627$ (viewed from three different perspectives).

The direction of maximum stretching is $\boldsymbol{e}_3$, the unit vector tangent to the ring centre circle, for $|\theta| \leqslant \pi/3$, and $\boldsymbol{e}_1$ otherwise. Fukumoto & Hattori (2002) calculated the probability distribution function of angles between the disturbance vorticity vector and the eigenvectors for the first principal mode at $(k_0, \omega_0) \approx (0.8134868347,$

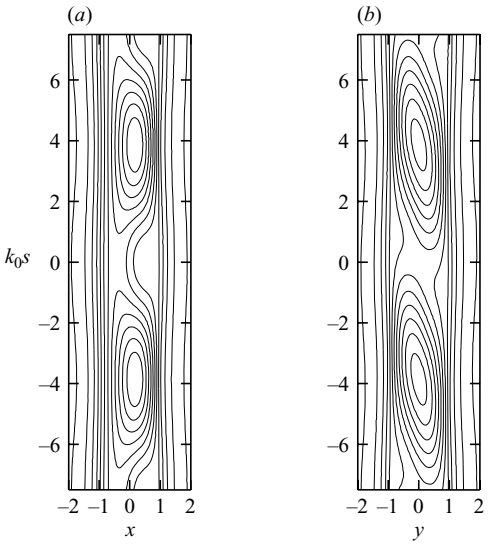

FIGURE 5. Contours of pressure in the section $\theta = \text{const.}$ for the first principal mode of the (0, 1) resonance excited at $(k_0, \omega_0) \approx (0.8134868347, 0.5970895378)$. $\epsilon = 0$. (*a*) $\theta = 0$, (*b*) $\theta = \pi/2$.

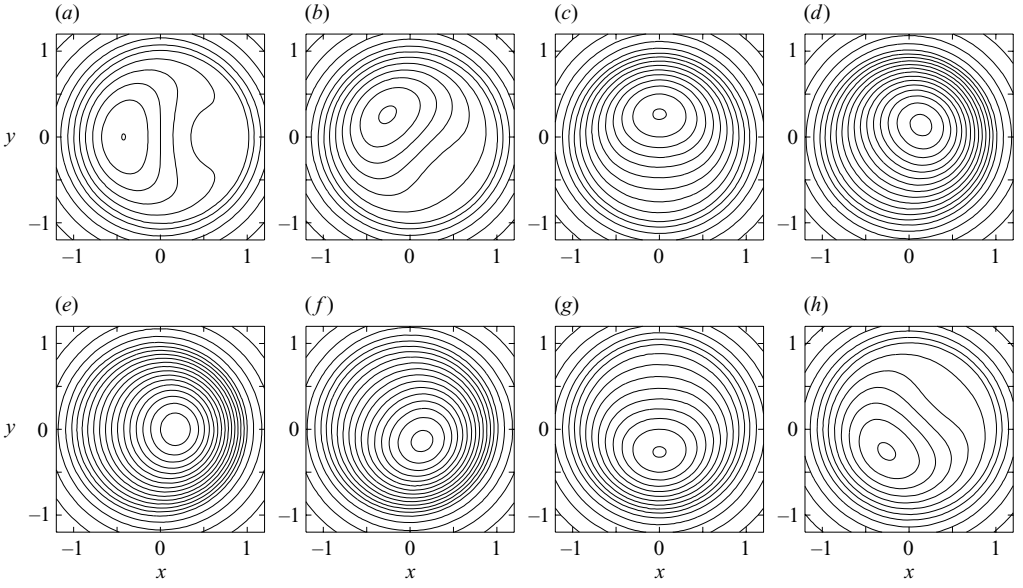

FIGURE 6. The same as figure 5 but on meridional planes. (*a*) $k_0 s = 0$, (*b*) $\pi/4$, (*c*) $\pi/2$, (*d*) $3\pi/4$, (*e*) π, (*f*) $5\pi/4$, (*g*) $3\pi/2$, (*h*) $7\pi/4$.

0.5970895378). A tendency of alignment of the vorticity vector was seen with $\boldsymbol{e}_3$ but not with $\boldsymbol{e}_1$. It is vortex-line stretching in the toroidal direction that plays the leading role of driving instability.

The magnitude of strain (4.3) increases with the distance r from the core centre and takes its maximum at the core boundary $r = 1$. In the geometric-optics approximation, the growth rate for the wave-packet disturbance of short wavelength attains its maximum on the streamline around the edge of the core (Hattori & Fukumoto 2003).

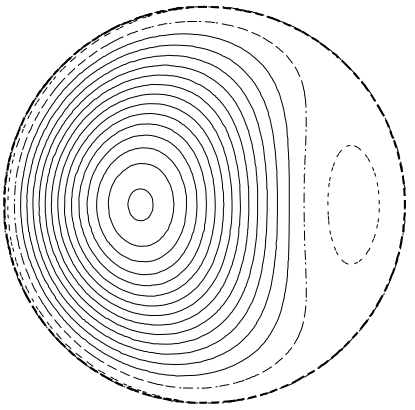

FIGURE 7. Contours of disturbance toroidal velocity field w_0 on the meridional plane $k_0 s = \omega_0 t$ for the first principal mode of the $(0, 1)$ resonance excited at $(k_0, \omega_0) \approx (0.8134868347, 0.5970895378)$. The outer dashed line depicts the core boundary $r = 1$.

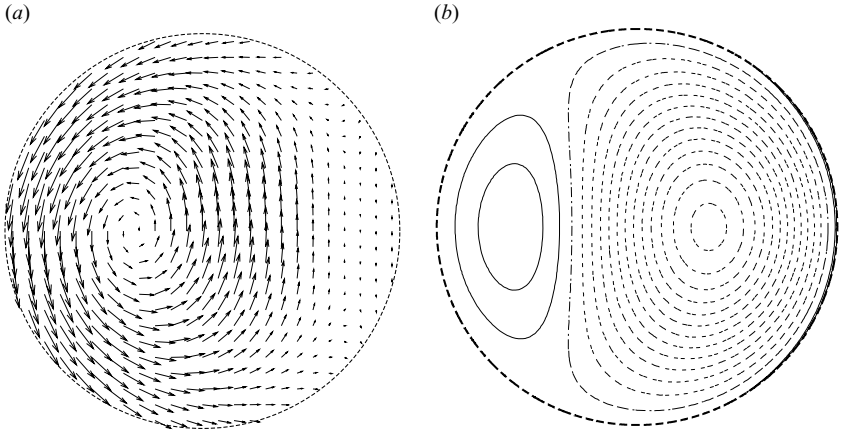

FIGURE 8. Disturbance vorticity field in the meridional plane $k_0 s = \omega_0 t$ of the first principal mode of the $(0, 1)$ resonance excited at $(k_0, \omega_0) \approx (0.8134868347, 0.5970895378)$. (a) The meridional components $(\omega_{0r}, \omega_{0\theta})$. (b) Contours of disturbance toroidal vorticity field ω_{0s}. The outer dashed line depicts the core boundary $r = 1$.

It follows that only the disturbance vorticity near the core boundary is relevant to the growth rate. In § 5.3, we will discuss disturbance vorticity of short wavelength at $r = 1$.

The growth rate of the principal modes diminishes as the branch label i becomes larger. Calculation of intersection points of the dispersion curves and of the growth rate at those points is extended to large wavenumbers and is plotted in figure 9. The growth rate stays at relatively large values along the two sequences of intersection points, rapidly converging to $\omega_0 = 0.5$ (figure 9a). One sequence is intersection points between the ith cograde mode of $m = 0$ and the ith retrograde mode of $m = 1$ for which the growth rate monotonically decreases with k_0, and the other sequence is a collection of intersection points between the $(i + 1)$th cograde mode of $m = 0$ and the ith retrograde mode of $m = 1$ for which the growth rate is, except for the first few intersection points, an increasing function of k_0. Eloy & Le Dizès (2001) called the latter the principal modes. We include both in the principal modes. Other

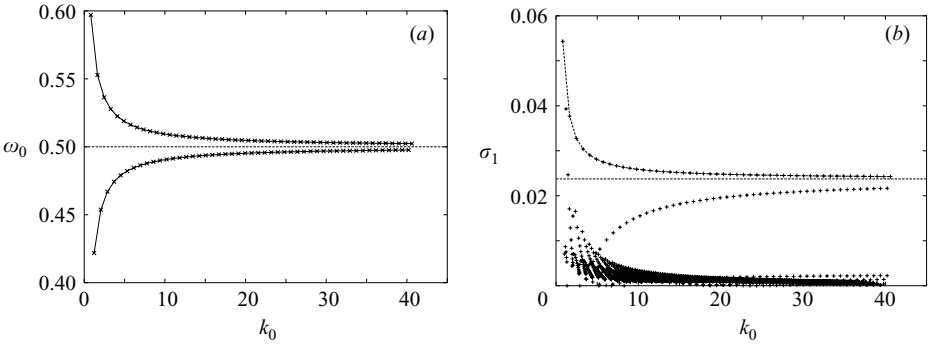

FIGURE 9. Large-wavenumber behaviour of the (0, 1) resonance. (*a*) The intersection points (k_0, ω_0) of the dispersion curves, (*b*) the maximum growth rate $\sigma_{1\max}$.

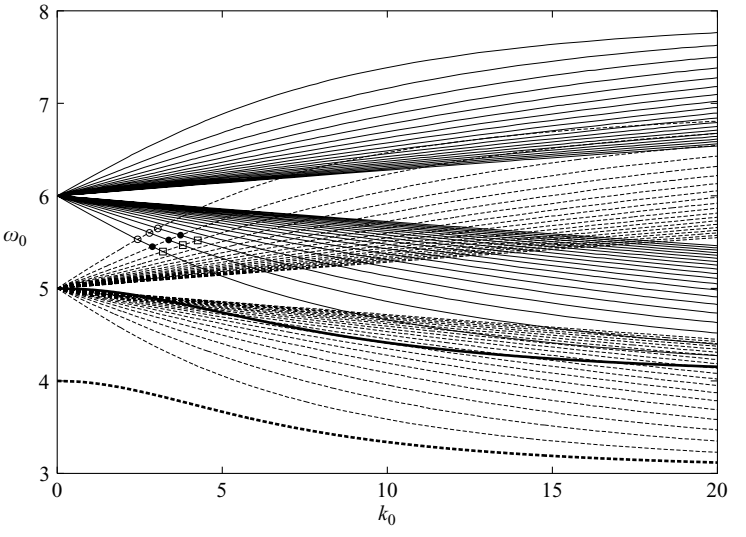

FIGURE 10. Dispersion relation of Kelvin waves of $m = 5$ (dashed lines) and $m = 6$ (solid lines) on the Rankine vortex. The isolated branches of $m = 5$ and $m = 6$ are shown with thick dashed and solid lines respectively.

sequences do not die away in the short-wave limit, though they are much less active. A mathematical analysis of the short-wavelength asymptotics is deferred to § 5, where the limiting value will be found to be $\sigma_{1\max} \approx 0.02374715242$ (the horizontal line in figure 9*b*).

4.2. *Resonance between the* 5, 6 *waves*

To exemplify higher-wave resonance, we select the coupling $(m, m+1) = (5, 6)$ waves. Their linear dispersion relation is drawn in figure 10, with dashed lines for $m = 5$ and solid lines for $m = 6$. The isolated branches are distinguished with thick lines.

The qualitative behaviour is no different from the 0, 1 waves. In the present case also, destabilization occurs only at the intersection points between the cograde radial modes of $m = 5$ and the retrograde radial modes of $m = 6$. The leftmost intersection $(k_0, \omega_0) = (0, 5)$ remains as a neutrally stable point as shown by (4.1).

Table 2 shows the growth rate $\sigma_{1\max}$ and the half-width Δk_1 at a few intersection points of low wavenumbers. The first three rows corresponds to the first three

k_0	ω_0	$\sigma_{1\max}$	Δk_1
2.433397462	5.529409164	0.3195204618	1.693646977
2.794997045	5.600007679	0.05182563467	0.3171404496
3.052129222	5.648538465	0.02232672268	0.1506487379
2.880420743	5.451428636	0.1240269171	0.7815646681
3.374566751	5.522917879	0.2216027292	1.624125748
3.737569089	5.573915602	0.04184266135	0.3403360657
3.202485864	5.397522759	0.05173895123	0.3663210904
3.804020554	5.467647077	0.1025219849	0.8482766785
4.255939038	5.519004934	0.1737789499	1.602267351

TABLE 2. The maximum growth rate $\epsilon\sigma_{1\max}$ and the half-width $\epsilon\Delta k_1$ of unstable wavenumber band to $O(\epsilon)$ for the (5,6) resonance. See text for details.

intersection points along the first cograde mode of $m=5$, which are marked with open circles in figure 10, the second three rows are along the second cograde mode (solid circles), and the last three rows along the third cograde mode (squares). A relatively large growth rate is maintained to short wavelengths at intersection points of the same branch labels. Continuing calculation to large wavenumbers, we find that the growth rate of the principal modes approaches $\sigma_{1\max}\approx 0.02374715242$ in common with the (0, 1) resonance (see § 5.1). The global maximum of the growth rate is at the first principal mode $(k_0,\omega_0)\approx(2.433397462, 5.529409164)$. It is noteworthy that the maximum value $\sigma_{1\max}\approx 0.3195204618$ for the (5, 6) resonance is substantially larger than $\sigma_{1\max}\approx 0.05434123370$ for the (0, 1) resonance. This contrasts with the MSTW instability for which the growth rate of the principal modes is insensitive to azimuthal wavenumber (Eloy & Le Dizès 2001; Fukumoto 2003).

For the first principal mode, the amplitude ratio of $m=6$ to $m=5$ modes is evaluated as $\beta^{(2)}/\beta^{(1)}\approx 0.9101456333$ to $O(\epsilon^0)$. Its core boundary and the pressure contours, on longitudinal planes, are shown in figures 11 and 12. The contours of disturbance toroidal velocity are depicted in figure 13, and the transversal disturbance vorticity field $(\omega_{0r},\omega_{0\theta})$ and the contours of disturbance toroidal vorticity ω_{0s} in figure 14. The azimuthal modal structure of $m=5$ and 6 is recognized. The toroidal velocity is enhanced around $\theta=\pi$, and correspondingly the toroidal vorticity is enhanced around $\theta=0$. The vigorous disturbance field is confined to an annular region near the edge of the core ($r=1$).

In order to grasp overall instability characteristics in the (k_0,ω_0)-space, a calculation of degenerate eigenvalues of the ith–ith radial modes of $(m, m+1)$ resonance is carried out over a wide range of k_0 and m. The growth rate is plotted in figure 15. The modes of $m=1, 2, \ldots, 10$ and $20, 30, \ldots, 60$ are shown. Given m, the growth rate of $(m, m+1)$ resonance decreases with the branch label i or the wavenumber k_0 and tends to $\sigma_{1\max}\approx 0.02374715242$ as $k_0\to\infty$. On the other hand, given the branch label, the growth rate increases monotonically with m and approaches $\sigma_{1\max}=0.64453125$ as $m\to\infty$. The ways of approaching the two different short-wave limits will be expounded in § 5.

4.3. *Energetics*

Krein's theory of Hamiltonian spectra underlies the preceding numerical results. A necessary condition for loss of stability at a double eigenvalue is either that the eigenfunction consists of waves with opposite signed energy or that the eigenvalue is 0

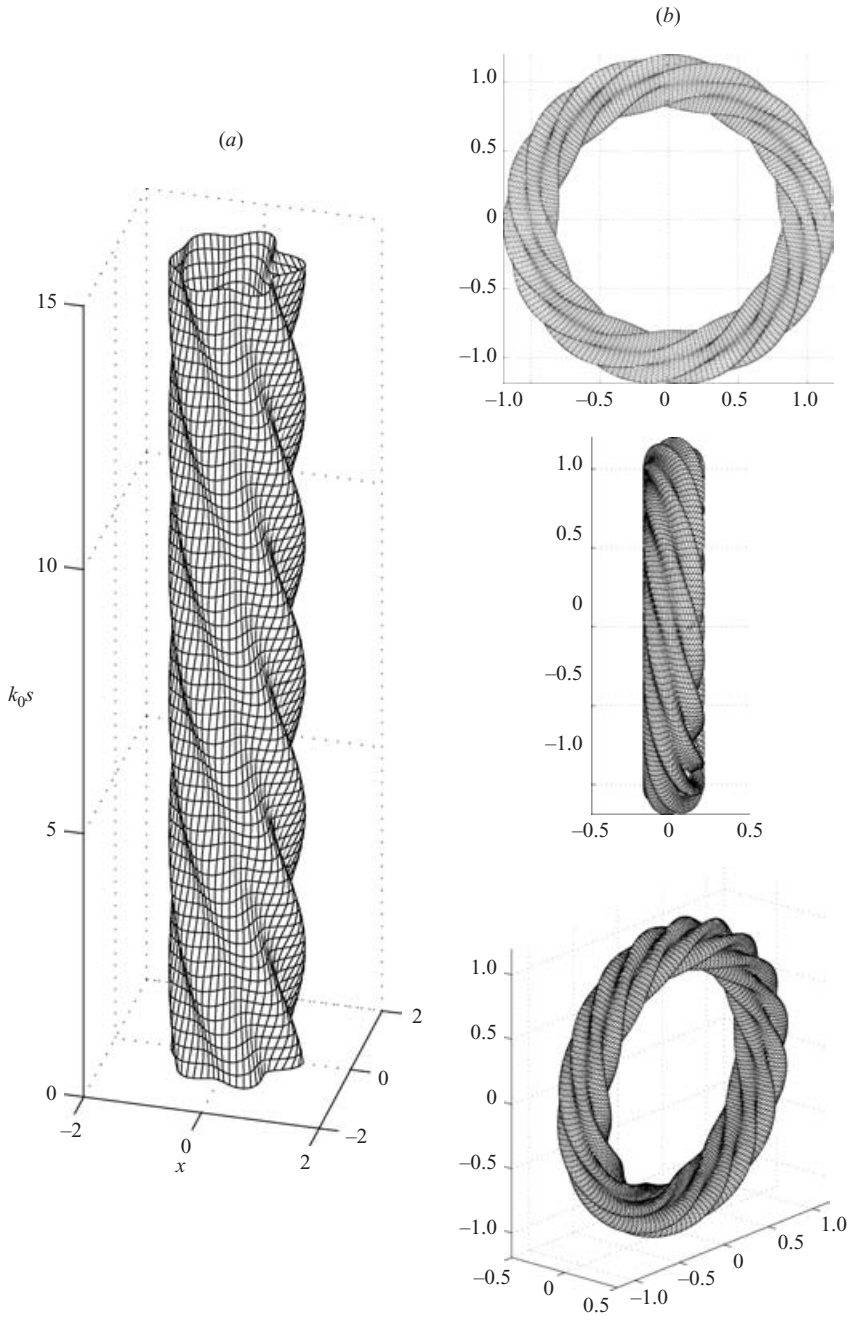

FIGURE 11. Shape of the disturbed vortex ring for the first principal mode of the (5, 6) resonance excited at $(k_0, \omega_0) \approx (2.433397462, 5.529409164)$. (*a*) $\epsilon = 0$, (*b*) $\epsilon = 0.1622$ (viewed from three different perspectives).

(MacKay 1986; Marsden 1992; Dellnitz, Melbourne & Marsden 1992; Guckenheimer & Mahalov 1992; Knobloch, Mahalov & Marsden 1994).

By taking advantage of Cairns' formula (Cairns 1979), Fukumoto (2003) obtained a neat expression for energy required to excite the Kelvin wave of azimuthal

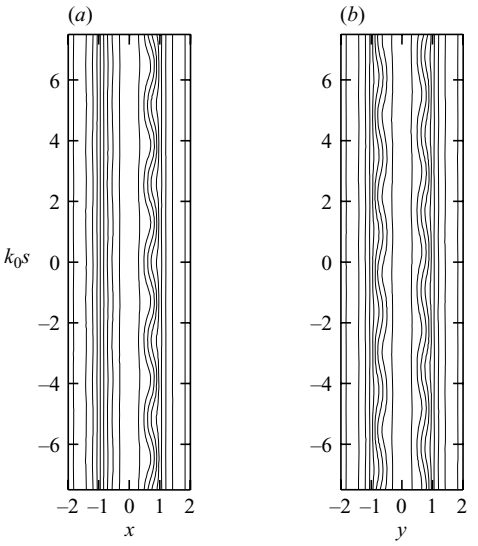

FIGURE 12. Contours of pressure in the section $\theta = \text{const.}$ for the first principal mode of the (5, 6) resonance excited at $(k_0, \omega_0) \approx (2.433397462, 5.529409164)$. $\epsilon = 0$. (*a*) $\theta = 0$, (*b*) $\theta = \pi/2$.

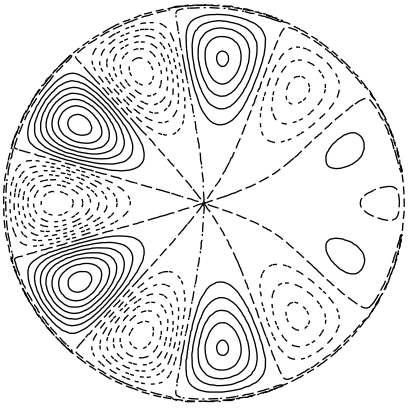

FIGURE 13. Contours of disturbance toroidal velocity field w_0 on the meridional plane $k_0 s = \omega_0 t$ for the first principal mode of the (5, 6) resonance excited at $(k_0, \omega_0) \approx (2.433397462, 5.529409164)$. The outer dashed line depicts the core boundary $r = 1$.

wavenumber m as

$$E = \frac{2\pi\omega_0}{\omega_0 - m}\left\{1 + \frac{(k_0/\eta_1)^2 K_{|m|}(k_0)}{k_0 K_{|m|-1}(k_0) + |m| K_{|m|}(k_0)}\left[\frac{2(\omega_0 + m)}{\omega_0 - m} + \left(\frac{m(\omega_0 + m)}{2} + k_0^2\right)\frac{K_{|m|}(k_0)}{k_0 K_{|m|-1}(k_0) + |m| K_{|m|}(k_0)}\right]\right\}\left(f_0^{(1)}\right)^2, \quad (4.5)$$

where $f_0^{(1)}$ is the displacement amplitude of the disturbed core $r = 1 + f_0^{(1)} \exp[\mathrm{i}(m\theta + k_0 z - \omega_0 t)]$, and is linked to the amplitude $\beta_0^{(1)}$ of the disturbance pressure through

$$f_0^{(1)} = \frac{1}{4 - (\omega_0 - m)^2}\left\{-\eta_m J_{|m|-1}(\eta_m) + \frac{|m|}{\omega_0 - m}\left(\omega_0 - m + \frac{2m}{|m|}\right) J_{|m|}(\eta_m)\right\}\beta_0^{(1)}. \quad (4.6)$$

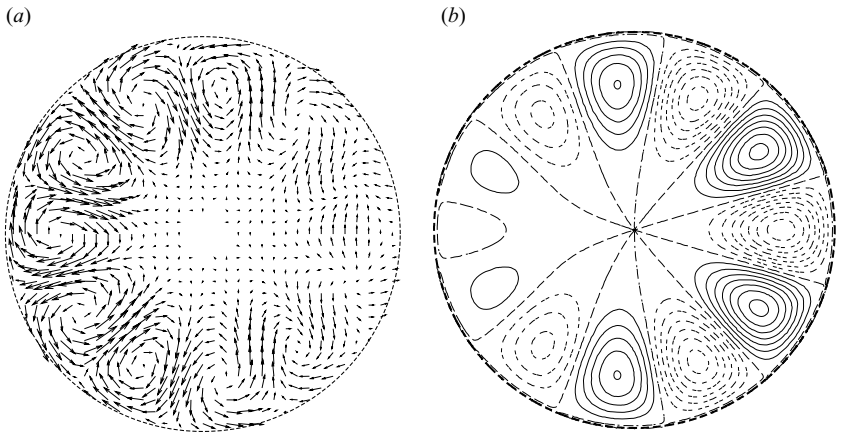

FIGURE 14. Disturbance vorticity field in the meridional plane $k_0 s = \omega_0 t$ of the first principal mode of the (5, 6) waves excited at $(k_0, \omega_0) \approx (2.433397462, 5.529409164)$. (*a*) The meridional components $(\omega_{0r}, \omega_{0\theta})$. (*b*) Contours of disturbance toroidal vorticity field ω_{0s}. The outer dashed line depicts the core boundary $r = 1$.

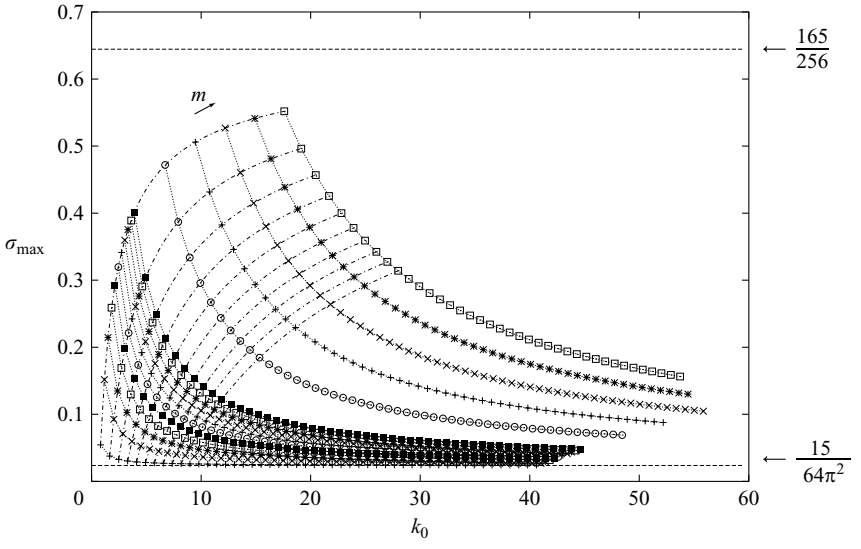

FIGURE 15. The growth rate of the principal resonance modes between the ith cograde modes of the m wave and the ith retrograde modes of the $m+1$ wave for $m = 1$–60. The same symbol is used for the same azimuthal wavenumber pair $(m, m+1)$. The lowest sequence represented by the symbol + corresponds to $m = 0$. The highest sequence represented by the symbol □ corresponds to $m = 60$.

Figure 16 shows graphs of Kelvin-wave energy, as a function of k_0, for the first few branches of (*a*) the axisymmetric wave $m = 0$ and, as an illustration for higher modes, (*b*) $m = 5$. Figure 16(*a*) shows the first five branches of $m = 0$ on the $\omega_0 > 0$ side. The energy of the axisymmetric wave is all positive, and, at a given k_0, the ith branch of the negative mode ($\omega_0 < 0$) has the same energy as the ith branch of the positive mode. For a fixed branch label i, the energy monotonically increases with k_0, while, given k_0, the energy decreases with branch label. The energy of the

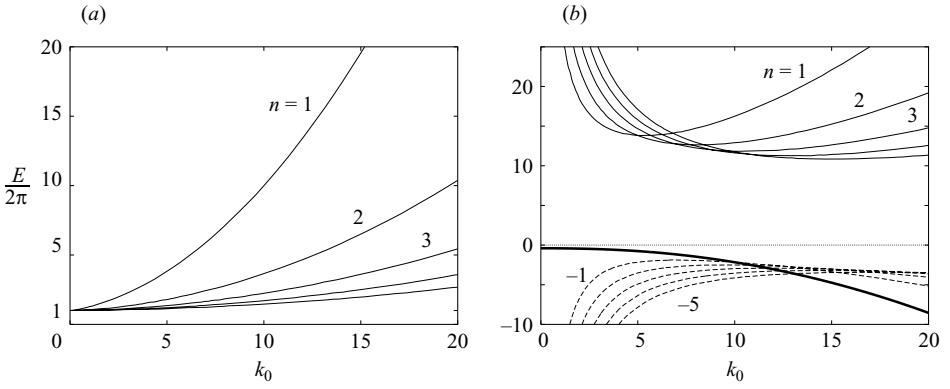

FIGURE 16. The wave energy E normalized by 2π, as a function of k_0, as given by (4.5) with $f_0^{(1)} = 1$. (*a*) The axisymmetric wave $m = 0$. The first five positive branches ($\omega_0 \geqslant 0$), labelled $n = 1, \ldots, 5$, are shown. (*b*) The $m = 5$ wave. The solid thick line corresponds to the isolated mode, dashed lines to the first five branches of retrograde radial modes ($|\omega_0| < 5$), labelled $n = -1, \ldots, -5$, and solid lines to the first five branches of cograde radial modes ($|\omega_0| > 5$), labelled $n = 1, \ldots, 5$.

bending wave ($m = 1$) was illustrated in figure 8 of Fukumoto (2003). The energy of the isolated mode and cograde radial modes of $m = 1$ is positive over the entire range of k_0, and therefore resonance with the $m = 0$ mode is ruled out. As is evident from (4.5), alteration of the energy sign occurs at the point, k_0^* say, where a dispersion curve crosses the k_0-axis. The energy of retrograde radial modes of $m = 1$ is negative in the range $0 < k_0 < k_0^*$, and is positive for $k_0 > k_0^*$. Eigenvalue collisions of negative- and positive-energy modes occur only between retrograde radial modes of $m = 1$ and upward modes of $m = 0$ in frequency range of $0 < \omega_0 < 1$, which is not in contradiction with the numerical example of § 4.1.

In figure 16(*b*) for $m = 5$, the thick line corresponds to the isolated mode, solid lines to the first five cograde radial modes labelled with $n = 1, \ldots, 5$, and dashed lines to the first five retrograde radial modes labelled with $n = -1, \ldots, -5$. The behaviour of energy curves of $m = 6$ does not differ from figure 16(*b*). A first glance shows us a simple rule for the energy sign. The energy of downward branches (the isolated mode and retrograde modes) is negative, whereas that of upward branches (cograde mode) is positive. It follows that eigenvalues of positive- and negative-energy modes meet only for a cograde mode of $m = 5$ and a retrograde mode of $m = 6$. These multiple eigenvalues lead to instability, with no exception.

Krein's criterion by means of the energy signature furnishes merely a necessary condition for instability, yet it in effect serves as a sufficient condition for instability as well. The same is true of the MSTW instability (Fukumoto 2003). The coincidence of the necessary condition with the sufficient condition is suggestive of the generic nature of the dipole field perturbation (2.7) in Krein's framework.

5. Short-wavelength asymptotics

The expression (3.23) for the growth rate suggests that a resonance pair with ω_0 closer to $m + 1/2$ is more influential. A universal feature manifests itself in the short-wavelength limit in which ω_0 converges to $m + 1/2$. We have two wavelengths at our disposal, namely the axial and the azimuthal wavelengths, and there are two ways

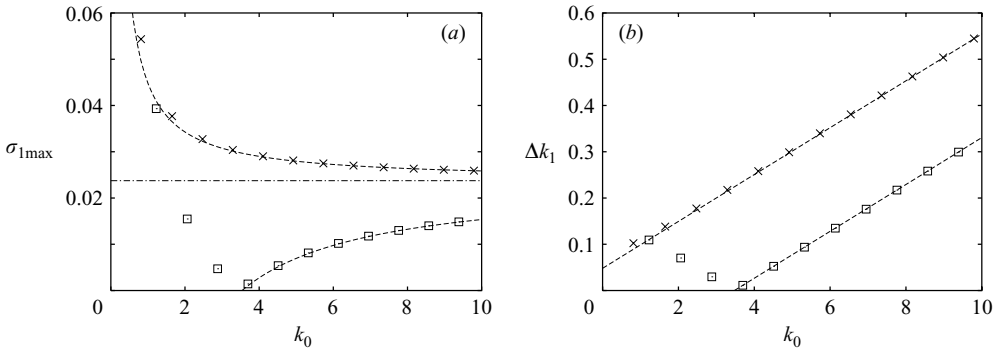

FIGURE 17. (*a*) The maximum growth rate $\sigma_{1\max}$ and (*b*) the half-width Δk_1 as functions of k_0 for the principal modes of (0, 1) resonance. □, $\Delta l = 0$; ×, $\Delta l = 1$. The short-wave asymptotics (5.2) and (5.3) are shown as dashed lines. The horizontal dashed line is the short-wave limit $\sigma_{1\max} = 15/(64\pi^2)$.

of taking the short-wavelength limit. We begin with a simple azimuthal structure by fixing m, and thereafter we turn to the limit of $m \to \infty$.

5.1. *Large k_0 with m fixed*

Asymptotic expansions of (k_0, ω_0) for degenerate eigenvalues of the $m, m+1$ waves are made in Appendix D. The intersection frequency ω_0 is given by (D 5), and the wavenumber k_0 by a solution of (D 7) for large integers l_1 and l_2 indexing branches of the m and the $m+1$ waves respectively.

Substituting from (D 5), (3.23) and (3.24) gives

$$\sigma_{1\max} = \frac{15}{64\pi^2(\Delta' l)^2} + \frac{\sqrt{15}}{32k_0}\left\{\frac{m}{\pi\Delta' l}\left[\frac{21}{8} + \frac{1}{\pi^2(\Delta' l)^2}\right] + \frac{1}{2}\left[-\frac{9\sqrt{15}}{64} + \frac{21}{8\pi\Delta' l} + \frac{\sqrt{15}}{16\pi^2(\Delta' l)^2} + \frac{1}{\pi^3(\Delta' l)^3}\right]\right\} + O\left(k_0^{-2}\right), \quad (5.1a)$$

$$\Delta k_1 = \frac{k_0}{2\pi^2(\Delta' l)^2} + \frac{m}{\sqrt{15}\pi\Delta' l}\left[\frac{21}{8} + \frac{1}{\pi^2(\Delta' l)^2}\right] + \frac{1}{2\sqrt{15}}\left[-\frac{9\sqrt{15}}{64} + \frac{21}{8\pi\Delta' l} + \frac{\sqrt{15}}{8\pi^2(\Delta' l)^2} + \frac{1}{\pi^3(\Delta' l)^3}\right] + O\left(k_0^{-1}\right), \quad (5.1b)$$

where the definition (D 6) for $\Delta' l = 2\Delta l - 1$ along with $\Delta l = l_2 - l_1$ is used. The finite value $15/(64\pi^2(\Delta' l)^2)$ of the growth rate is the asymptote in the limit of $k_0 \to \infty$, among which the modes specified by $\Delta l = 0$ and 1 have the largest growth rate $15/(64\pi^2) \approx 0.02374715242$. This limiting value is shared by all resonant pairs $(m, m+1)$ for finite values of m. These are the principal modes with slightly larger growth rate for $\Delta l = 1$. Correspondingly, the eigenfrequency ω_0 of the principal modes with $\Delta l = 0, 1$ attains a relatively rapid convergence to the limit $\omega_0 = m + 1/2$ from below and above respectively as is seen from (D 5) and is exemplified in figure 9(*a*) for the (0, 1) resonance. The unstable wavenumber band, to leading order, broadens linearly in k_0, and this broad-band nature guarantees the validity of the geometric optics approach used by Hattori & Fukumoto (2003).

Variation of the maximum growth rate $\sigma_{1\max}$ and the half-width Δk_1 of the unstable band with k_0 is shown for the (0, 1) resonance in figure 17. The principal mode with $\Delta l = 0$ is plotted with squares and that with $\Delta l = 1$ is plotted with crosses. The

short-wavelength asymptotics are obtained by choosing $m=0$ in (5.1). They become, for $\Delta l=1$,

$$\left.\begin{aligned}\sigma_{1\max} &\approx 0.02374715242+0.02104135307/k_0,\\ \Delta k_1 &\approx 0.05066059182\ k_0+0.04805450688,\end{aligned}\right\} \tag{5.2}$$

and, for $\Delta l=0$,

$$\left.\begin{aligned}\sigma_{1\max} &\approx 0.02374715242-0.08399092777/k_0,\\ \Delta k_1 &\approx 0.05066059182\ k_0-0.1760143589,\end{aligned}\right\} \tag{5.3}$$

and are drawn with dashed lines. They fit fairly well even at moderate wavenumbers, as small as $k_0\approx 3$ say.

Taking a careful look at figure 9(*b*) for the (0, 1) resonance, it is seen that modes other than the principal ones survive in the limit of $k_0\to\infty$, which is confirmed from (5.1). In harmony with this, the way of approaching $\omega_0=m+1/2$, as given by (D5), is of $O(k_0^{-1})$ for all values of Δl with $m/\Delta' l$ finite. This situation is contrasted with the MSTW instability for which the $\Delta l=0$ mode has a special status (Eloy & Le Dizès 2001; Fukumoto 2003).

Notice that the coefficients of the correction terms in the asymptotic expansions (5.1), (D 5) and (D 7) grow with m, being indicative of non-uniformity in the expansions. At large values of m, a new regime appears, in which vigorous modes reside.

5.2. *Large k_0 and m with $\eta_1\sim\eta_2\sim m$*

As $m\to\infty$, the intersection points (k_0,ω_0) between cograde radial modes of m and retrograde radial modes of $m+1$ are arranged so as to satisfy $\eta_1\sim\eta_2\sim m$ (Eloy & Le Dizès 2001). The asymptotic expansions for (k_0,ω_0) for those points are given, to a high order in $1/m^{1/3}$, as (D 15) and (D 16) in Appendix D.2. In these, $a_1(<0)$ and $a_2(<0)$ are the zeros of the Airy function Ai and play the role of the branch labels for the m and the $m+1$ waves respectively. The first zero $a_1\approx -2.338107410$ is linked to the first cograde radial mode of m and $a_2\approx -2.338107410$ to the first retrograde radial mode of $m+1$.

A rapid approach to $\omega_0=m+1/2$ as $m\to\infty$ demands $\Delta a=a_2-a_1=0$. They are at the crossing points between the ith branches of both m and $m+1$ radial waves, and thus are inherited from the principal modes of $\Delta l=1$. The growth rate and the unstable bandwidth for the case of $\Delta a=0$ are, from (3.23) and (3.24),

$$\sigma_{1\max}=\frac{165}{256}\left(1-\frac{33499\,|a_1|}{25872\times 2^{1/3}m^{2/3}}\right)+O(m^{-1}), \tag{5.4}$$

$$\Delta k_1=\frac{11}{8\sqrt{15}}\,m\left(1-\frac{7627\,|a_1|}{25872\times 2^{1/3}m^{2/3}}\right)+O(m^{0}). \tag{5.5}$$

The common value $\sigma_{1\max}=165/256$ is the asymptote. Among them, the longest-wave pair with $a_1=a_2\approx -2.338107410$, the first principal mode, has the largest growth rate:

$$\sigma_{1\max}\approx 0.64453125-1.548698742/m^{2/3}, \tag{5.6}$$

$$\Delta k_1\approx 0.3550234734\,m-0.1942235728\,m^{1/3}. \tag{5.7}$$

This is the most dominant mode of all possible resonance pairs. The increase, with m, of growth rate for the first principal mode is illustrated, with crosses, to $m=60$ in figure 18. Squares are asymptotic expansions (5.6) with k_0 given by (D 15).

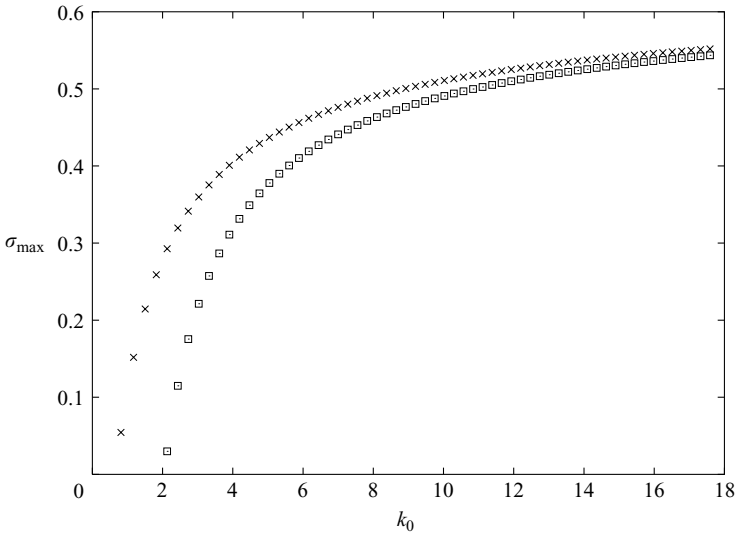

FIGURE 18. Variation of the maximum growth rate $\sigma_{1\max}$ with m for the resonance between the first-first radial modes of the m, $m+1$ waves, shown with $\times$. $m = 1, 2, \ldots, 60$. The short-wave asymptotics (5.6) and (D 15) are shown with $\square$.

It is worth noting that the limit $\sigma_{1\max} = 165/256$ coincides with the value obtained by Hattori & Fukumoto (2003) through the geometric optics approach of Lifschitz & Hameiri (1991). The present solution supplies us with its structure globally in space. Recall that the angle between the normal to a streamline and the wave vector of the WKB ansatz projected onto a meridional plane, at the initial instant, was denoted ϕ. This limit corresponds to $\phi = \pi/2$ and therefore the projected wave vector is parallel to the streamline. On the other hand, the orthogonal case $\phi = 0$ corresponds to the preceding limit of fixed m, for which growth rate of the global mode is reduced from the local one by factor $(\pi/2)^{-2}$ as

$$\sigma_{1\max} \to \frac{15\epsilon}{256}\left(\frac{\pi}{2}\right)^{-2} \quad \text{as} \quad k_0 \to \infty \quad \text{with } m \text{ fixed}, \tag{5.8}$$

for a reason unknown to us. These correspondences are understood by recalling that $\phi \sim \tan^{-1} C' m/\eta_i^{2/3}$ in the present case and $\phi \sim \tan^{-1} Cm/\eta_i$ in the preceding case (Hattori & Fukumoto 2003) for some constants C and C'; note that, for the present limit, the 'effective' wavenumber in the radial direction is estimated as $\eta_i J_m'(\eta_i r)/J_m(\eta_i r) \sim \eta_i^{2/3}$ for $1 - r = O(m^{1/3})$ (Abramowitz & Stegun 1965). Incidentally, the same factor $(\pi/2)^{-2}$ was derived in the case of a planar hexapole perturbation, being proportional to $\cos 3\theta$ and $\sin 3\theta$, by Eloy & Le Dizès (2001).

In the case $\Delta a = a_2 - a_1 \neq 0$, convergence of the eigenvalue to $\omega_0 = m + 1/2$ is slower. Consequently the resonance instability is weaker as is seen from

$$\sigma_{1\max} = \frac{4365}{3584 \times 2^{2/3}\,|\Delta a|\, m^{1/3}}\left\{1 + \frac{7627}{4074 \times 2^{2/3}\Delta a\, m^{1/3}}\right\} + O(m^{-1}), \tag{5.9}$$

$$\Delta k_1 = \frac{97}{112 \times 2^{2/3}}\sqrt{\frac{3}{5}}\frac{m^{2/3}}{|\Delta a|}\left\{1 + \frac{7627}{4074 \times 2^{2/3}\Delta a\, m^{1/3}}\right\} + O(m^0). \tag{5.10}$$

This mode is suppressed in the limit of $m \to \infty$.

5.3. *Disturbance vorticity at the edge of the core*

The local rate of strain (4.3) is strengthened in proportion to the distance r from the core centre. Accordingly, the growth rate of a short-wavelength disturbance is proportional to r and attains its maximum at the edge $r=1$ of the core. We highlight vortex-line stretching on the core boundary $r=1$.

5.3.1. *Disturbance vorticity at $r=1$ when $k\to\infty$ with m fixed*

First, we consider the asymptotic behaviour of the disturbance vorticity at the edge of the core ($r=1-0$) when $k\to\infty$ but with m fixed. Our attention is focused on the degenerate eigenvalues of $\Delta l=l_2-l_1=1$

The limiting behaviour of the ratio of the pressure coefficient is

$$\frac{\beta_0^{(2)}}{\beta_0^{(1)}}=1+O\left(k_0^{-1}\right). \tag{5.11}$$

Substituting from (5.11) and formulae in Appendices B and D.1, the limit of (3.10) is evaluated at $r=1$. Set

$$\hat{\beta}_0=-16k_0^2\beta_0^{(1)}\sqrt{\frac{2}{\sqrt{15}\pi k_0}}\cos\left(\eta_1-\frac{(2m+1)\pi}{4}\right). \tag{5.12}$$

The disturbance vorticity $\nabla\times\boldsymbol{v}_0\exp[\mathrm{i}(k_0s-\omega_0t)]$ of $O(\epsilon^0)$ evaluated at $r=1$ is written to leading order, in components in the toroidal coordinates (r,θ,s), as

$$\tilde{\boldsymbol{\omega}}_0|_{r=1-0}\approx\hat{\beta}_0\begin{pmatrix}-\sin\Theta\cos\frac{1}{2}\theta\\ 4\sin\Theta\sin\frac{1}{2}\theta\\ \cos\Theta\cos\frac{1}{2}\theta\end{pmatrix}, \tag{5.13}$$

where

$$\Theta=\left(m+\tfrac{1}{2}\right)\theta+k_0s-\omega_0t. \tag{5.14}$$

5.3.2. *Disturbance vorticity at $r=1$ when $m\sim\eta_1\sim\eta_2\to\infty$*

Next we turn to the most unstable modes of $m\sim\eta_1\sim\eta_2\to\infty$. For clarity, we confine ourselves to the dominant case of $\Delta a=a_2-a_1=0$. In this limit,

$$\frac{\beta_0^{(2)}}{\beta_0^{(1)}}=1+O\left(m^{-4/3}\right). \tag{5.15}$$

Substituting from (5.15) and formulae in Appendix D.2, the disturbance vorticity, when the boundary $r=1$ is approached from inside, is reduced to

$$\tilde{\boldsymbol{\omega}}_0|_{r=1-0}\approx\tilde{\beta}_0\left\{\cos\Theta\begin{pmatrix}-4\sin\frac{1}{2}\theta\\ -\cos\frac{1}{2}\theta\\ \sqrt{15}\cos\frac{1}{2}\theta\end{pmatrix}+\sin\Theta\begin{pmatrix}-4\sqrt{15}\cos\frac{1}{2}\theta\\ 15\sqrt{15}\sin\frac{1}{2}\theta\\ -\sin\frac{1}{2}\theta\end{pmatrix}\right\}, \tag{5.16}$$

where

$$\tilde{\beta}_0=\frac{2^{4/3}m^{4/3}}{105}\mathrm{Ai}'(a_1)\beta_0^{(1)}, \tag{5.17}$$

with $\mathrm{Ai}'(x)$ being differentiation of $\mathrm{Ai}(x)$ in x.

Comparison of (5.16) with (5.13) shows that the large-m limit gives an additional degree of freedom to the eigenfunction. Conceivably the augmented freedom renders the vorticity vector liable to the stretching action of the straining field (4.3).

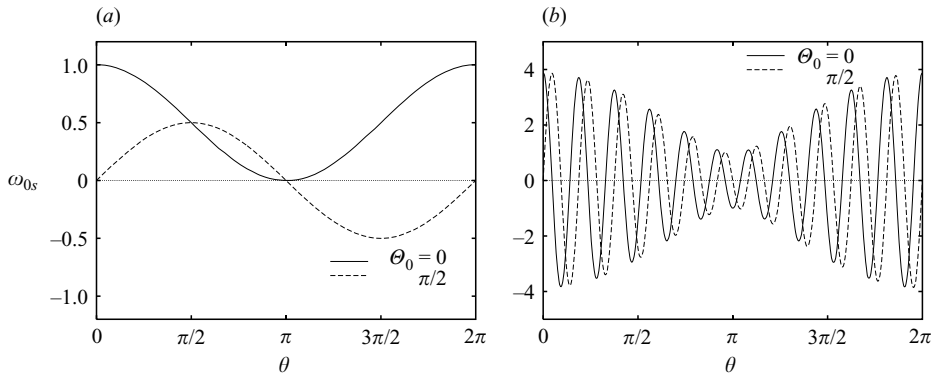

FIGURE 19. The toroidal component $\tilde{\omega}_{0s}$ of disturbance vorticity at the boundary $r = 1 - 0$ of the core. (*a*) The short-wavelength limit with m maintained finite as given by (5.13). We choose $m = 0$. (*b*) The limit of $m \sim \eta_1 \sim \eta_2 \to \infty$ as given by (5.16). We choose $m = 10$. In both (*a*) and (*b*), the solid line is the curve of $\tilde{\omega}_{0s}|_{r=1}$ as a function of θ for the phase $\Theta_0 = k_0 s - \omega_0 t = 0$ and the dashed line is for the phase $\Theta_0 = \pi/2$.

Figure 19(*a*, *b*) depict the variation of the toroidal disturbance vorticity $\tilde{\omega}_{0s}$ along the peripheral circle $r = 1 - 0$ in the limit of $k_0 \to \infty$ with m fixed and in the limit of $m \sim \eta_1 \sim \eta_2 \to \infty$, respectively. Figure 19(*a*) corresponds to the (0, 1) resonance, and only one wavelength is contained. As is obtained from (4.3), the toroidal strain is $x = \cos\theta$. Positive strain in the toroidal direction is largest at $\theta = 0$, monotonically decreases with θ, changes its sign at $\theta = \pi/2$ and reaches the minimum value at $\theta = \pi$. When $\Theta_0 = k_0 s - \omega_0 t = 0$, the toroidal vorticity takes a configuration susceptible to amplification by stretching (the solid line), but, when $\Theta_0 = \pi/2$, the configuration is out of phase with the stretching action (the broken line). In figure 19(*b*), $\tilde{\omega}_{0s}$ given by (5.16) is shown with the choice of $m = 10$. The toroidal vorticity exploits the doubled degrees of freedom to adjust itself to comply, at every phase, with the stretching action of the strain.

6. Effect of elliptical deformation and viscosity

It is generally agreed that the elliptical deformation of the core is responsible for instability. However the local pure shear appears at second order in ϵ, whereas the curvature effect in question is of $O(\epsilon)$. We now inquire into the practical relevance of the curvature effect.

6.1. *Inviscid case*

We again take the distribution vorticity to be linear in distance from the axis of symmetry, though the growth rate and the unstable mode of the $O(\epsilon)$ effect sensitively depend on the vorticity distribution as demonstrated by Hattori & Fukumoto (2003). Kelvin's vortex ring is the first-order truncation of asymptotic expansions of the Euler equations, and a higher-order extension of expansions was accomplished by Dyson (1893) (see also Fraenkel 1972; Fukumoto & Moffatt 2000 and Fukumoto 2002). This represents a thin limit of the Fraenkel–Norbury family (Fraenkel 1970; Norbury 1973). Roughly speaking, the second-order term is looked upon as a pure shear flow of strength

$$\frac{3\Gamma}{16\pi R^2}\left[\log\left(\frac{8}{\epsilon}\right) - \frac{17}{12}\right], \tag{6.1}$$

in terms of dimensional variables (Saffman 1978).

WT77 calculated the $O(\epsilon^2)$ straining-field effect. For instance, the growth rate $\epsilon^2\sigma_{2\max}$ corresponding to the stationary mode with the simplest radial structure of the MSTW instability is

$$\sigma_{2\max} \approx \sqrt{\left[0.428\log\left(\frac{8}{\epsilon}\right) - 0.4549\right]^2 - 0.1134}. \tag{6.2}$$

When ϵ is large, this mode becomes competitive with the principal modes of $O(\epsilon)$.

The second-order growth rate $\sigma_{2\max}$ monotonically increases as ϵ is increased from zero, takes the maximum value $\sigma_{2\max} \approx 0.338$ at $\epsilon \approx 0.660$, and then monotonically decreases with ϵ. For the first principal mode of the (6, 7) pair, $\sigma_{1\max} \approx 0.3414099690$ and $\sigma_{1\max}$ is larger for larger azimuthal-wavenumber pairs $(m, m+1)$ (see figure 18). It follows that $\epsilon\sigma_{1\max} > \epsilon^2\sigma_{2\max}$ within the range of $0 < \epsilon < 1$. Being limited to lower azimuthal wavenumbers, $\epsilon\sigma_{1\max} > \epsilon^2\sigma_{2\max}$ when $\epsilon \lesssim 0.0281$ for the (0, 1) resonance, $\epsilon \lesssim 0.116$ for (1, 2), $\epsilon \lesssim 0.200$ for (2, 3), $\epsilon \lesssim 0.283$ for (3, 4), $\epsilon \lesssim 0.369$ for (4, 5), and $\epsilon \lesssim 0.471$ for (5, 6). At large values of ϵ, $\epsilon\sigma_{1\max} > \epsilon^2\sigma_{2\max}$. For the (5, 6) pair, this occurs for $\epsilon \gtrsim 0.850$. Our asymptotic expansion cannot be justifiably applied in this range.

This overall comparison implies that the $O(\epsilon)$ curvature effect exerts a major influence, but the situation may not be that simple.

6.2. *Viscous case*

So far we have ignored the action of viscosity. The eigenvalues for the first principal modes are arranged in a sequence of the intersection points of the dispersion curves that are extended to the range of large radial, azimuthal and toroidal wavenumbers η_1, m and k_0, and hence these modes entail substantial viscous dissipation.

Incorporating viscosity requires that we tackle the Navier–Stokes equations. A reasonably systematic procedure of incorporating small viscosity, equivalent to the treatment of Eloy & Le Dizès (2001), is given in Appendix C, and the inviscid formula (3.23) is replaced by

$$\epsilon\sigma^v_{1\max} = \left\{\epsilon^2\sigma^2_{1\max} + \frac{4\pi^2k_0^4}{R_\Gamma^2}\left(\frac{\Delta^{(1)}}{f^{(1)}} - \frac{\Delta^{(2)}}{f^{(2)}}\right)^2\right\}^{1/2} - \frac{2\pi k_0^2}{R_\Gamma}\left(\frac{\Delta^{(1)}}{f^{(1)}} + \frac{\Delta^{(2)}}{f^{(2)}}\right), \tag{6.3}$$

where $\Delta^{(1)}$ and $\Delta^{(2)}$ are defined by (C 19) and (C 20) respectively, and R_Γ is the circulation Reynolds number (3.1).

We restrict attention to the first principal modes. The curvature effect cannot overcome the viscous damping effect at small Reynolds numbers. When R_Γ exceeds $899.9024378/\epsilon$, only the (1, 2) mode can be sustained. When R_Γ exceeds $1048.733698/\epsilon$, the (2, 3) mode becomes excited and, when $R_\Gamma \approx 1401.899548/\epsilon$, catches up with the (1, 2) mode. As R_Γ increases, the dominant mode is successively taken by a higher azimuthal-wavenumber mode. There is no parameter region for which the (0, 1) mode is the strongest.

If we choose, for instance, $R_\Gamma = 10000$ and $\epsilon = 0.2$, the largest growth rate $\sigma^v_{1\max} \approx 0.1010467686$ is attained for the (2, 3) mode. The growth rate of subdominant modes, $\sigma^v_{1\max} \approx 0.09310201142$ for the (3, 4) mode and $\sigma^v_{1\max} \approx 0.08239309841$ for the (1, 2) mode, is not very different. Since the principal (2, 3), (3, 4) and (1, 2) modes are excited at $k_0 \approx 1.503834658$, 1.821017959 and 1.173528968, the number of waves round one circuit of the ring is $k/\epsilon \approx 8$, 9 and 6 respectively.

A rather good approximation to (6.3) is supplied by

$$\epsilon\sigma^{v}_{1\max} \approx \epsilon\sigma_{1\max} - \frac{2\pi}{R_\Gamma}\left[k_0^2 + (m+1)^2 + \eta_1^2\right]. \tag{6.4}$$

Inclusion of the radial wavenumber η_1 signifies that, due to the finer radial structure, the $O(\epsilon)$ instability is more susceptible to viscous damping than the $O(\epsilon^2)$ instability, if the axial wavenumber k_0 is the same. This is because $\eta_1 \sim \sqrt{15}k_0$ for the principal modes of the $O(\epsilon)$ instability, while $\eta_1 \sim \sqrt{3}k_0$ for those of the MSTW instability.

At a high Reynolds number to be discussed subsequently in comparison with the $O(\epsilon)$ effect, the dominant unstable mode caused by the $O(\epsilon^2)$ plane straining field would be the first stationary helical–helical wave resonance, though the 0, 2-pair is relatively strengthened as the viscosity is increased (Eloy & Le Dizès 2001). By virtue of the symmetry of the $m = \pm 1$ modes, the resulting expression for dimensionless growth rate $\sigma^{v}_{2\max}$ takes a neat form:

$$\epsilon^2\sigma^{v}_{2\max} = \epsilon^2\sigma_{2\max} - \frac{4\pi k_0^2}{R_\Gamma}\frac{\Delta^{(1)}}{f^{(1)}}, \tag{6.5}$$

where $\sigma_{2\max}$ is substituted from (6.2) and

$$f^{(1)} = 6\left(\frac{k_0K_0}{K_1}\right)^2 + \frac{8k_0K_0}{K_1} + 2k_0^2 + 3, \tag{6.6}$$

$$\Delta^{(1)} = 12\left(\frac{k_0K_0}{K_1}\right)^2 + \frac{13k_0K_0}{K_1} + 4k_0^2 + 3, \tag{6.7}$$

are obtained from (C 13) and (C 19) by setting $m = -1$ and $\omega_0 = 0$. The wavenumber to be substituted is $k_0 \approx 2.505$ for the simplest radial mode. The $O(\epsilon^2)$ instability does not demand short wavelengths. The viscosity acts in favour of the straining effect, and the second-order effect overturns the first-order one when R_Γ is not very large.

Based on our model, we divide the parameter space (ϵ, R_Γ) into the regions dominated by one of the modes under consideration as shown in figure 20. The solid lines are concerned with the $O(\epsilon)$ instability modes. The left-hand thick line is the cut-off curve $R_\Gamma \approx 899.9024378/\epsilon$, below which all modes are damped. At $(\epsilon, R_\Gamma) \approx (0.1265, 7115)$, this is replaced by the cut-off curve of the $O(\epsilon^2)$ first helical–helical wave resonance (the lower thick line). The band bounded by the thick line and the adjacent line is the region where the (1, 2) mode is dominant, and is then followed by the dominant region of the (2, 3) mode in increasing order in R_Γ. The right-hand thick line with R_Γ increasing with ϵ, except at smaller ϵ, is the critical line for competition between the first- and the second-order effects, to the left of which the $O(\epsilon)$ effect surpasses the $O(\epsilon^2)$ effect. For $R_\Gamma \lesssim 10000$, the range of ϵ dominated by the $O(\epsilon)$ effect is not wide, but it expands with R_Γ for $R_\Gamma \gtrsim 10000$.

Our procedure is not complete, because the underlying steady flow (2.6) and (2.7) does not satisfy the Navier–Stokes equations. The Gaussian distribution of vorticity could be taken as a model for vortex rings in a practical situation (Weigand & Gharib 1997), though a broader distribution is envisaged by Maxworthy (1972, 1977) and Saffman (1978). The local stability analysis of Hattori & Fukumoto (2003) shows that the growth rate $\sigma_{1\max}$ corresponding to the limit of $k_0 \to \infty$ with m fixed is larger for the Gaussian core than for the uniform core. This result may have some implications for the practical relevance of the curvature effect, if the above-mentioned cases of finite m have a link with this limit. However, care should be exercised. The exponentially growing instability, on average, corresponding to the limit of $m \sim \eta_1 \sim \eta_2 \to \infty$

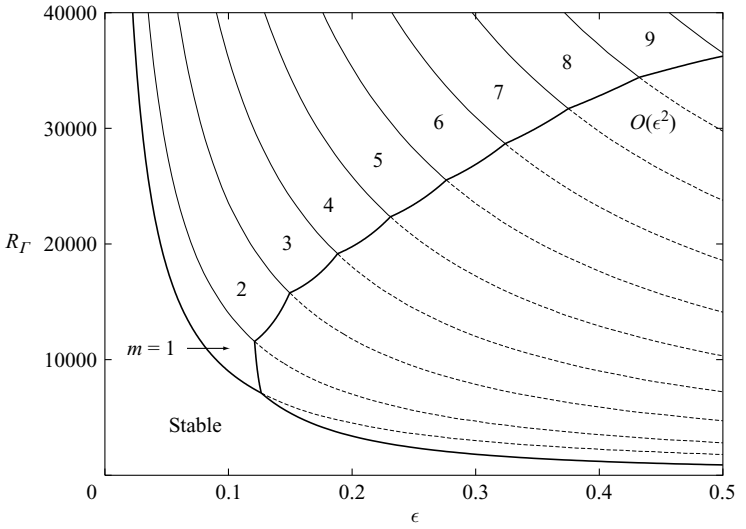

FIGURE 20. The regions dominated by one of the $(m, m+1)$ modes of the $O(\epsilon)$ effect. The left-hand thick solid line is the cut-off curve below which no growing mode of $O(\epsilon)$ is permitted. The azimuthal wavenumber m of the dominant mode $(m, m+1)$ is indicated. The right-hand thick line is the critical one, the right-hand side of which is superseded by the $O(\epsilon^2)$ effect.

disappears for the Gaussian core. A global stability analysis of the Gaussian core is left for a future study (cf. Eloy & Le Dizès 1999).

7. Conclusion

We have addressed the question of whether the $O(\epsilon)$ dipole field, the leading-order effect of vortex-line curvature in Kelvin's vortex ring, can bring about parametric resonance between Kelvin waves whose azimuthal wavenumbers are separated by one. The answer is positive. The influence of the quadrupole field of $O(\epsilon^2)$ has been thoroughly studied since the pioneering work of Widnall *et al.* (1974) and is now understood within the category of the elliptical instability. Although the dipole field precedes the quadrupole field, in the asymptotic solution of the Euler and the Navier–Stokes equations, the former has attracted little attention. The dipole field also plays the role of symmetry-breaking perturbations in the framework of Krein's theory for Hamiltonian systems (MacKay 1986; Dellnitz, *et al.* 1992). One difference is that, for the $O(\epsilon)$ instability, eigenvalue collision of Kelvin waves does not necessarily lead to instability. This is not the case with the MSTW instability of $O(\epsilon^2)$. The energetics accounts for this difference.

In passing we point out that the Coriolis force acting on a circulatory flow is also viewed locally as a dipole field. The resonance between the m and the $m+1$ Kelvin waves, mediated by the Coriolis force, was investigated by Kerswell (1993), Mahalov (1993) and Mason & Kerswell (2002).

Formally the dipole field is more influential than the quadrupole field by one order in ϵ, but comparison requires numerical values of the growth rate. We have succeeded in deriving formulae for the growth rate and the unstable bandwidth in closed form in terms of the modified Bessel functions, from which the short-wavelength asymptotics are deduced at once. The most unstable mode resides in the short-wavelength limit

of $m \sim \eta_1 \sim \eta_2 \to \infty$, and its growth rate is $\sigma_{1\max} = 165/256$, in accordance with the value obtained, through the geometric optics approach, by Hattori & Fukumoto (2003). Being restricted to the inviscid uniform core, $\epsilon\sigma_{1\max}$ exceeds $\epsilon^2\sigma_{2\max}$ for the whole range of possible values of ϵ, $0 < \epsilon < 1$ say. But they are rather competitive. Viscosity damps preferentially the $O(\epsilon)$ curvature effect because the wavelength of the dominant modes of $O(\epsilon)$ is short in all spatial directions and because, given the axial wavenumber k_0, the radial wavenumber is larger for the $O(\epsilon)$ mode. For fat cores, the MSTW instability may predominate. The critical value of ϵ depends on R_Γ, and the relative importance of the $O(\epsilon)$ effect is more and more pronounced as R_Γ is larger.

The mechanism of the $O(\epsilon)$ instability is attributable to vortex-line stretching by the dipole field. The straining field (4.3) is not confined to the meridional plane, and toroidal vortex lines undergo stretching on the front side of torus. In contrast to plane pure shear, strain is strengthened as the core boundary $r = 1$ is approached, and as a consequence the most unstable mode concentrates vorticity near the boundary of the convex side. The alignment of vorticity vector with stretching direction at $r = 1 - 0$ is achieved only in the toroidal direction as verified by the neat form (5.16) of the vorticity asymptotics as $m \sim \eta_1 \sim \eta_2 \to \infty$.

Unlike the MSTW or the elliptical instability, the $O(\epsilon)$ instability result is highly sensitive to the vorticity distribution as the local rate of strain varies from place to place. The uniform vorticity in the core to $O(\epsilon^0)$ does not faithfully mimic vortex rings in practical flows. The vorticity is peaked near $r = 0$, decreasing with r, and the region of large strain is located closer to the core centre. According to Hattori & Fukumoto's short-wavelength analysis, the Gaussian vorticity distribution eliminates the instability mode corresponding to the limit of $m \sim \eta_1 \sim \eta_2 \to \infty$, but accentuates the mode corresponding to the limit of $k_0 \to \infty$ with m fixed. We expect that resonance modes of finite m could be amplified for a peaked vorticity distribution, compared with a uniform one. However, the global stability of a vortex ring with distributed vorticity is not a straightforward extrapolation of the present result. Even spectra on a circular-cylindrical vortex tube are yet to be determined. Not only discrete spectra but also continuous spectra will take part in the dynamics and smear out Krein's picture for parametric resonance.

At present, no experimental evidence is available that can be tied to the $(m, m+1)$ resonance. Shariff, Verzicco & Orlandi (1994) conducted an elaborated numerical simulation of three-dimensional vortex ring instabilities. Lead by the intuition of Widnall *et al.* (1974), they focused their modal analyses on the stationary modes, and left aside the non-stationary instability modes. Krasny, Lindsay & Nitsche (2002) extended the vortex blob method to three dimensions, and thereby computed the development of an undulation on the toroidal core formed by rolling up a cylindrical vortex sheet. In their simulation, the number of waves is prescribed by the initial disturbance, and remains unaltered throughout the temporal evolution. The same is true of the experiment by Naitoh *et al.* (2002). If the growth rate did not differ much among vigorous instability modes, the initial condition would have a decisive influence on modal selection. The (0,1) resonance represents a helically winding axial flow. Naitoh *et al.* (2002) claimed that the genesis of observed axial flow stems from nonlinear process when the elliptical instability reaches a mature stage. Yet a possibility might not be ruled out that the $(0, 1)$ resonance serves as a seed for it. Lugomer & Fukumoto (2005) found possible evidence for this resonance in vortex rings of micron scale generated by a laser–matter interaction. But to discriminate the instability driven by the dipole field from others is not straightforward. Direct

numerical simulation of the Navier–Stokes equations is called for in order to obtain evidence for the $O(\epsilon)$ instability.

Our explicit solution of the linear stability problem is helpful in making headway in solving nonlinear modal interactions. The form of equations describing weakly nonlinear evolution is available in the framework of the normal form theory as developed by Guckenheimer & Mahalov (1992) and Knobloch *et al.* (1994). Our solution will render feasible efficient and accurate calculation of their coefficients.

The present investigation rests on a particular solution of the Euler equations, Kelvin's vortex ring. This model may be too simplified to have much bearing on instability and disruption of vortex rings in a realistic situation. We have clarified, at least, that a vortex ring accommodates rich wavy structures of various origin. Hopefully this paper serves as a stepping stone for an understanding of the evolution of vortex rings in nature.

Y. F. was supported in part by a Grant-in-Aid for Scientific Research from the Japan Society for the Promotion of Science.

Appendix A. Navier–Stokes equations in moving toroidal coordinates

In this appendix, we list the dimensionless equations written in the moving toroidal coordinates (r, θ, s) defined by (2.3) and shown in figure 1. Refer to WT77 for the details of the derivation.

An irrotational flow is a solution of the Navier–Stokes equations. The Laplace equation for the velocity potential ϕ outside the core is

$$\nabla^2\phi = \frac{1}{r}\frac{\partial}{\partial r}\left(r\frac{\partial\phi}{\partial r}\right) + \frac{1}{r^2}\frac{\partial^2\phi}{\partial\theta^2} + \frac{1}{h_s^2}\frac{\partial^2\phi}{\partial s^2} + \frac{\epsilon}{h_s}\left(\sin\theta\frac{\partial\phi}{\partial r} + \frac{\cos\theta}{r}\frac{\partial\phi}{\partial\theta}\right) = 0, \quad \text{(A 1)}$$

where

$$h_s = 1 + \epsilon r\sin\theta. \quad \text{(A 2)}$$

The Navier–Stokes equations to be solved inside the core are written in component form as

$$\frac{\partial u}{\partial t} + (\boldsymbol{v}\cdot\nabla)u - \frac{v^2}{r} - \frac{\epsilon w^2\sin\theta}{h_s} = -\frac{\partial p}{\partial r} + \frac{2\pi}{R_\Gamma}\left\{\nabla^2 u - \frac{u}{r^2} - \frac{2}{r^2}\frac{\partial v}{\partial\theta} - \frac{\epsilon v\cos\theta}{h_s r} - \frac{2\epsilon\sin\theta}{h_s^2}\frac{\partial w}{\partial s} - \frac{\epsilon^2}{h_s^2}\sin\theta(u\sin\theta + v\cos\theta)\right\}, \quad \text{(A 3)}$$

$$\frac{\partial v}{\partial t} + (\boldsymbol{v}\cdot\nabla)v + \frac{uv}{r} - \frac{\epsilon w^2\cos\theta}{h_s} = -\frac{1}{r}\frac{\partial p}{\partial\theta} + \frac{2\pi}{R_\Gamma}\left\{\nabla^2 v - \frac{v}{r^2} + \frac{2}{r^2}\frac{\partial u}{\partial\theta} + \frac{\epsilon\cos\theta u}{h_s r} - \frac{2\epsilon\cos\theta}{h_s^2}\frac{\partial w}{\partial s} - \frac{\epsilon^2}{h_s^2}\cos\theta(u\sin\theta + v\cos\theta)\right\}, \quad \text{(A 4)}$$

$$\frac{\partial w}{\partial t} + (\boldsymbol{v}\cdot\nabla)w + \frac{\epsilon}{h_s}w(u\sin\theta + v\cos\theta) = -\frac{1}{h_s}\frac{\partial p}{\partial s} + \frac{2\pi}{R_\Gamma}\left\{\nabla^2 w + \frac{2\epsilon}{h_s^2}\left(\frac{\partial u}{\partial s}\sin\theta + \frac{\partial v}{\partial s}\cos\theta\right) - \frac{\epsilon^2 w}{h_s^2}\right\}, \quad \text{(A 5)}$$

where R_Γ is the circulation Reynolds number defined by (3.1) and

$$\boldsymbol{v}\cdot\nabla = u\frac{\partial}{\partial r} + \frac{v}{r}\frac{\partial}{\partial\theta} + \frac{w}{h_s}\frac{\partial}{\partial s}. \tag{A 6}$$

The equation of continuity is

$$\nabla\cdot\boldsymbol{v} = \frac{1}{r}\frac{\partial}{\partial r}(ru) + \frac{1}{r}\frac{\partial v}{\partial\theta} + \frac{1}{h_s}\frac{\partial w}{\partial s} + \frac{\epsilon}{h_s}(u\sin\theta + v\cos\theta) = 0. \tag{A 7}$$

Appendix B. Kelvin waves

The expressions for the velocity field and the dispersion relation of Kelvin waves are collected in this appendix. The details are found, for example, in Tsai & Widnall (1976), Kopiev & Chernyshev (1997) and Fukumoto (2003).

The leading-order disturbance flow field of azimuthal wavenumber m is obtained in the form of normal mode as

$$\boldsymbol{v}_0 = \boldsymbol{v}_0^{(1)}(r)\,\mathrm{e}^{\mathrm{i}m\theta}, \quad \pi_0 = \pi_0^{(1)}(r)\,\mathrm{e}^{\mathrm{i}m\theta}, \quad \phi_0 = \phi_0^{(1)}(r)\,\mathrm{e}^{\mathrm{i}m\theta}. \tag{B 1}$$

By separately integrating the linearized Euler equations outside and inside the core with radius given by (2.11) we find that

$$\phi_0^{(1)} = K_m(k_0 r)\alpha_0^{(1)} \qquad \text{for} \quad r > 1 + \tilde{f}_0, \tag{B 2}$$

and

$$\left.\begin{aligned}
\pi_0^{(1)} &= J_m(\eta_1 r)\beta_0^{(1)},\\
u_0^{(1)} &= \frac{\mathrm{i}}{\omega_0 - m + 2}\left\{-\frac{m}{r}J_m(\eta_1 r) + \frac{\omega_0 - m}{\omega_0 - m - 2}\eta_1 J_{m+1}(\eta_1 r)\right\}\beta_0^{(1)},\\
v_0^{(1)} &= \frac{1}{\omega_0 - m + 2}\left\{\frac{m}{r}J_m(\eta_1 r) + \frac{2}{\omega_0 - m - 2}\eta_1 J_{m+1}(\eta_1 r)\right\}\beta_0^{(1)},\\
w_0^{(1)} &= \frac{k_0}{\omega_0 - m}J_m(\eta_1 r)\beta_0^{(1)}\\
&\qquad\qquad\qquad\qquad \text{for} \quad r < 1 + \tilde{f}_0,
\end{aligned}\right\} \tag{B 3}$$

where the radial wavenumber η_1 is given by

$$\eta_1^2 = [4/(\omega_0 - m)^2 - 1]k_0^2, \tag{B 4}$$

and J_m and K_m are respectively the Bessel function of the first kind and the modified Bessel function of the second kind, m being their order, and $\alpha_0^{(1)}$ and $\beta_0^{(1)}$ are arbitrary constants. The non-singular conditions $\omega_0 \neq m$ and $\omega_0 \neq m \pm 2$ are to be kept in view.

The boundary conditions supply the relation between $\alpha_0^{(1)}$ and $\beta_0^{(1)}$ as

$$\alpha_0^{(1)} = -\frac{\mathrm{i}J_m(\eta_1)}{(\omega_0 - m)K_m(k_0)}\beta_0^{(1)}, \tag{B 5}$$

and the dispersion relation

$$J_{m+1}(\eta_1) = \left\{\frac{2m}{\omega_0 - m + 2} - \frac{k_0 K_{m+1}(k_0)}{K_m(k_0)}\right\}\frac{\eta_1}{k_0^2}J_m(\eta_1). \tag{B 6}$$

The dispersion relation for a Kelvin wave of azimuthal wavenumber $m+1$ is

$$J_m(\eta_2) = \left\{ \frac{k_0 K_m(k_0)}{K_{m+1}(k_0)} - \frac{2(m+1)}{\omega_0 - m - 3} \right\} \frac{\eta_2}{k_0^2} J_{m+1}(\eta_2), \tag{B 7}$$

and is also used to simplify the boundary conditions at $O(\epsilon)$ (Appendix C). Here η_2 is the radial wavenumber of the $m+1$ wave given by

$$\eta_2^2 = [4/(\omega_0 - m - 1)^2 - 1]k_0^2. \tag{B 8}$$

The corresponding amplitude functions $\boldsymbol{v}_0^{(2)}(r)$ and $\pi_0^{(2)}(r)$ of the velocity field should be expressed in terms of $J_m(\eta_2)$ and $J_{m+1}(\eta_2)$.

Appendix C. Closed-form solution for disturbance field and the solvability conditions

This appendix is concerned with the closed-form solution of the $O(\epsilon)$ disturbance field, the boundary conditions, and the solvability conditions for a possible parametric resonance between Kelvin waves with azimuthal wavenumbers m and $m+1$. The superscript 1 refers to the m wave, and 2 refers to the $m+1$ wave.

By inspection and with the help of computer algebra, a general solution of (3.18) for the m wave, finite at $r=0$, is manipulated to give

$$\begin{aligned}
\pi_1^{(1)} = {} & J_m(\eta_1 r)\beta_1^{(1)} + \left\{ \frac{4k_0^2\omega_1}{(\omega_0 - m)^3} - \frac{\eta_1^2 k_1}{k_0} \right\} \frac{r}{\eta_1} J_{m+1}(\eta_1 r)\beta_0^{(1)} \\
& + \frac{\mathrm{i}}{16} \left\{ \left[5(r^2-1) + \frac{(\omega_0 - m - 1)^2(\omega_0 - m)^2(\omega_0 - m + 2)}{2k_0^2(2\omega_0 - 2m - 1)^2(\omega_0 - m + 1)} A_1 \right] \eta_2 J_m(\eta_2 r) \right. \\
& \left. + \frac{A_2}{2\omega_0 - 2m - 1} r J_{m+1}(\eta_2 r) \right\} \beta_0^{(2)} + \frac{16 i \tilde{\nu} k_0^4}{(\omega_0 - m)^5 \eta_1} r J_{m+1}(\eta_1 r)\beta_0^{(1)},
\end{aligned} \tag{C 1}$$

where $\beta_1^{(1)}$ is a constant and

$$\left.\begin{aligned}
A_1 = {} & 9\omega_0^4 - 18(2m+1)\omega_0^3 + (54m^2 + 54m + 1)\omega_0^2 \\
& - 2(2m+1)(3m-2)(3m+5)\omega_0 + 9m^4 + 18m^3 - 23m^2 - 32m - 8, \\
A_2 = {} & 9\omega_0^4 - 9(4m+1)\omega_0^3 + (54m^2 + 27m - 26)\omega_0^2 \\
& - (36m^3 + 27m^2 - 56m - 20)\omega_0 + 9m^4 + 9m^3 - 30m^2 - 22m - 2.
\end{aligned}\right\} \tag{C 2}$$

Returning to the Euler equations (3.2) and (3.3), the disturbance radial velocity $u_1^{(1)}$ is found to be

$$\begin{aligned}
u_1^{(1)} = {} & \mathrm{i} \left\{ -\frac{m J_m(\eta_1 r)}{(\omega_0 - m + 2)r} + \frac{1}{2} \left(\frac{1}{\omega_0 - m + 2} + \frac{1}{\omega_0 - m - 2} \right) \eta_1 J_{m+1}(\eta_1 r) \right\} \beta_1^{(1)} \\
& + \frac{\mathrm{i}\omega_1}{(\omega_0 - m + 2)^2} \left\{ \left[\frac{m}{r} + \frac{4\eta_1^2 r}{(\omega_0 - m - 2)^2} \right] J_m(\eta_1 r) \right. \\
& \left. - \frac{1}{(\omega_0 - m - 2)^2} \left[\omega_0^2 - 2m\omega_0 + (m+2)^2 + \frac{8m}{\omega_0 - m} \right] \eta_1 J_{m+1}(\eta_1 r) \right\} \beta_0^{(1)} \\
& - \mathrm{i}k_1 \left\{ \frac{k_0}{\omega_0 - m} r J_m(\eta_1 r) + \frac{m}{k_0(\omega_0 - m - 2)} \eta_1 J_{m+1}(\eta_1 r) \right\} \beta_0^{(1)} \\
& + \frac{1}{16} \left\{ \frac{1}{\omega_0 - m + 1} \left[m \left(\frac{(\omega_0 - m)^2(\omega_0 - m - 1)^2}{2k_0^2(2\omega_0 - 2m - 1)^2} A_1 - 5 \right) \frac{1}{r} \right. \right. \\
& \left. \left. + \frac{A_3}{(\omega_0 - m - 3)(2\omega_0 - 2m - 1)} r \right] \eta_2 J_m(\eta_2 r) \right.
\end{aligned}$$

$$+\left[\frac{A_4}{2(\omega_0-m-3)(2\omega_0-2m-1)^2}+\frac{5k_0^2}{\omega_0-m-1}(r^2-1)\right]J_{m+1}(\eta_2 r)\Bigg\}\beta_0^{(2)},$$
$$-\frac{4\tilde{\nu}k_0^2}{(\omega_0-m)^2(\omega_0-m+2)^2}\Bigg\{\left[m-\frac{4(\omega_0-m+2)k_0^2r^2}{(\omega_0-m)^2(\omega_0-m-2)}\right]\frac{J_m(\eta_1 r)}{r}$$
$$-\frac{\omega_0^3-3m\omega_0^2+(3m^2+4m+4)\omega_0-m(m^2+4m-4)}{(\omega_0-m)(\omega_0-m-2)^2}\eta_1 J_{m+1}(\eta_1 r)\Bigg\}\beta_0^{(1)}, \quad (C\,3)$$

where

$$A_3=9\omega_0^5-9(5m+3)\omega_0^4+(90m^2+108m+1)\omega_0^3-(90m^3+162m^2-11m-11)\omega_0^2$$
$$+(45m^4+108m^3-25m^2-63m+14)\omega_0-9m^5-27m^4+13m^3+52m^2+3m-8,$$
$$A_4=9\omega_0^8-18(4m+3)\omega_0^7+2(126m^2+189m+41)\omega_0^6-2(252m^3+567m^2$$
$$+252m-8)\omega_0^5+(630m^4+1890m^3+1290m^2-98m-87)\omega_0^4$$
$$-2(252m^5+945m^4+880m^3-116m^2-262m-27)\omega_0^3$$
$$+2(126m^6+567m^5+675m^4-134m^3-533m^2-154m+18)\omega_0^2$$
$$-2(36m^7+189m^6+276m^5-76m^4-454m^3-235m^2+32m+28)\omega_0$$
$$+9m^8+54m^7+94m^6-34m^5-279m^4-216m^3+24m^2+68m+16. \quad (C\,4)$$

Likewise, for the $m+1$ wave, we have

$$\pi_1^{(2)}=J_{m+1}(\eta_2 r)\beta_1^{(2)}-\left\{\frac{4k_0^2\omega_1}{(\omega_0-m-1)^3}-\frac{\eta_2^2k_1}{k_0}\right\}\frac{r}{\eta_2}J_m(\eta_2 r)\beta_0^{(2)}$$
$$+\frac{\mathrm{i}}{16}\Bigg\{\left[\frac{A_2}{2\omega_0-2m-1}-9\omega_0^2+9(2m+1)\omega_0-9m^2-9m+8\right]rJ_m(\eta_1 r)$$
$$+\left[5(r^2-1)+\frac{(\omega_0-m-1)^2(\omega_0-m)^2(\omega_0-m-3)}{2k_0^2(2\omega_0-2m-1)^2(\omega_0-m-2)}A_1\right]\eta_1 J_{m+1}(\eta_1 r)\Bigg\}\beta_0^{(1)}$$
$$-\frac{16\mathrm{i}\tilde{\nu}k_0^4}{(\omega_0-m-1)^5\eta_2}rJ_m(\eta_2 r)\beta_0^{(2)}, \quad (C\,5)$$

and

$$u_1^{(2)}=\mathrm{i}\Bigg\{-\frac{1}{2}\left(\frac{1}{\omega_0-m+1}+\frac{1}{\omega_0-m-3}\right)\eta_2 J_m(\eta_2 r)+\frac{(m+1)J_{m+1}(\eta_2 r)}{(\omega_0-m-3)r}\Bigg\}\beta_1^{(2)}$$
$$+\frac{\mathrm{i}\omega_1}{(\omega_0-m-3)^2}\Bigg\{\frac{1}{(\omega_0-m+1)^2}\left[\omega_0^2-2(m+1)\omega_0+(m-1)^2+\frac{8(m+1)}{\omega_0-m-1}\right]$$
$$\times\eta_2 J_m(\eta_2 r)-\left[\frac{m+1}{r}-\frac{4\eta_2^2 r}{(\omega_0-m+1)^2}\right]J_{m+1}(\eta_2 r)\Bigg\}\beta_0^{(2)}$$
$$-\mathrm{i}k_1\Bigg\{\frac{m+1}{k_0(\omega_0-m+1)}\eta_2 J_m(\eta_2 r)+\frac{k_0}{\omega_0-m-1}rJ_{m+1}(\eta_2 r)\Bigg\}\beta_0^{(2)}$$
$$-\frac{1}{16}\Bigg\{\frac{1}{\omega_0-m+2}\left[\frac{A_4}{2(2\omega_0-2m-1)^2}+\frac{1}{4}\left(2\omega_0-2m-1-\frac{5}{2\omega_0-2m-1}\right)A_1\right.$$
$$\left.-4(2m+1)+5k_0^2\left(1+\frac{2}{\omega_0-m}\right)(r^2-1)\right]J_m(\eta_1 r)$$
$$+\frac{1}{\omega_0-m-2}\left[(m+1)\left(\frac{(\omega_0-m)^2(\omega_0-m-1)^2}{2k_0^2(2\omega_0-2m-1)^2}A_1-5\right)\frac{1}{r}\right.$$

$$+\frac{A_3+A_1+3\left[20\omega_0^2-15(2m+1)\omega_0+10m^2+10m+2\right]}{(\omega_0-m+2)(2\omega_0-2m-1)}r\Bigg]\eta_1 J_{m+1}(\eta_1 r)\Bigg\}\beta_0^{(1)}$$
$$-\frac{4\tilde{\nu}k_0^2}{(\omega_0-m-1)^2(\omega_0-m-3)^2}$$
$$\times\left\{\frac{\omega_0^3-3(m+1)\omega_0^2+(3m^2+2m+3)\omega_0-(m+1)(m^2-2m-7)}{(\omega_0-m-1)(\omega_0-m+1)^2}\eta_2 J_m(\eta_2 r)\right.$$
$$\left.-\left[m+1+\frac{4(\omega_0-m-3)k_0^2r^2}{(\omega_0-m-1)^2(\omega_0-m+1)}\right]\frac{J_{m+1}(\eta_2 r)}{r}\right\}\beta_0^{(2)}, \tag{C 6}$$

where $\beta_1^{(2)}$ is a constant.

Substituting from (3.16), (C 1), (C 3) and the expressions in Appendix B and evaluating them at $r=1$, the boundary conditions (3.21) for the m wave are converted into linear algebraic equations for $\alpha_1^{(1)}$ and $\beta_1^{(1)}$:

$$\begin{bmatrix} mK_m-k_0K_{m+1} & \dfrac{\mathrm{i}}{\omega_0-m+2}\left[mJ_m(\eta_1)-\dfrac{\omega_0-m}{\omega_0-m-2}\eta_1 J_{m+1}(\eta_1)\right] \\ -\mathrm{i}(\omega_0-m)K_m & J_m(\eta_1) \end{bmatrix}\begin{bmatrix}\alpha_1^{(1)}\\ \beta_1^{(1)}\end{bmatrix}=\begin{bmatrix}F^{(1)}\\ G^{(1)}\end{bmatrix}, \tag{C 7}$$

where we have made use of the shorthand notation $K_m=K_m(k_0)$ and $K_{m+1}=K_{m+1}(k_0)$. The dispersion relation (B 6) helps to simplify $F^{(1)}$ and $G^{(1)}$ by eliminating $J_{m+1}(\eta_1)$ from these equations. The boundary conditions (3.22) for the $m+1$ wave give linear algebraic equations for $\alpha_1^{(2)}$ and $\beta_1^{(2)}$:

$$\begin{bmatrix} -[k_0K_m+(m+1)k_0K_{m+1}] & \dfrac{\mathrm{i}}{\omega_0-m-3}\left[\dfrac{\omega_0-m-1}{\omega_0-m+1}\eta_2 J_m(\eta_2)-(m+1)J_{m+1}(\eta_2)\right] \\ -\mathrm{i}(\omega_0-m-1)K_{m+1} & J_{m+1}(\eta_2) \end{bmatrix}$$
$$\times\begin{bmatrix}\alpha_1^{(2)}\\ \beta_1^{(2)}\end{bmatrix}=\begin{bmatrix}F^{(2)}\\ G^{(2)}\end{bmatrix}. \tag{C 8}$$

Elimination of $J_m(\eta_2)$, by use of (B 7), achieves simplification of $F^{(2)}$ and $G^{(2)}$.

As is usually the case, the matrix in (C 7) is singular, and hence the vector $(F^{(1)}, G^{(1)})$ must be constrained to its image space in order for (C 7) to be solvable for $(\alpha_1^{(1)}, \beta_1^{(1)})$. This solvability condition is

$$\mathrm{i}(\omega_0-m)F^{(1)}+\left(m-\frac{k_0K_{m+1}}{K_m}\right)G^{(1)}=0. \tag{C 9}$$

The solvability condition for the $m+1$ wave is

$$\mathrm{i}(\omega_0-m-1)F^{(2)}-\left(m+1+\frac{k_0K_m}{K_{m+1}}\right)G^{(2)}=0. \tag{C 10}$$

These conditions are rewritten into homogeneous linear algebraic equations for $\beta_0^{(1)}$ and $\beta_0^{(2)}$ as

$$\left\{\omega_1 f^{(1)}+\frac{2k_1}{k_0}(\omega_0-m)(\omega_0-m+2)(\omega_0-m-2)g^{(1)}+2\mathrm{i}\tilde{\nu}k_0^2\Delta^{(1)}\right\}\beta_0^{(1)}$$
$$+\frac{\mathrm{i}(\omega_0-m)^4(\omega_0-m+2)(\omega_0-m-2)J_{m+1}(\eta_2)}{32k_0^2(2\omega_0-2m-1)^2(\omega_0-m-1)J_m(\eta_1)}h\beta_0^{(2)}=0, \tag{C 11}$$

$$-\frac{\mathrm{i}(\omega_0-m-1)^4(\omega_0-m+1)(\omega_0-m-3)J_m(\eta_1)}{32k_0^2(2\omega_0-2m-1)^2(\omega_0-m)J_{m+1}(\eta_2)}h\beta_0^{(1)}$$
$$+\left\{\omega_1 f^{(2)}+\frac{2k_1}{k_0}(\omega_0-m-1)(\omega_0-m+1)(\omega_0-m-3)g^{(2)}+2\mathrm{i}\tilde{\nu}k_0^2\Delta^{(2)}\right\}\beta_0^{(2)}=0. \tag{C 12}$$

In these,

$$f^{(1)}=m\left[\omega_0^3-(3m+4)\omega_0^2+3m^2\omega_0-m(m^2-4m-8)\right]+2k_0^2(\omega_0-m)^2$$
$$+4\left[(m+1)\omega_0^2-2m^2\omega_0+m(m^2-m-4)\right]\frac{k_0K_{m+1}}{K_m}$$
$$-2(\omega_0-m+2)(\omega_0-m-2)\frac{k_0^2K_{m+1}^2}{K_m^2}, \tag{C 13}$$

$$f^{(2)}=(m+1)\left[\omega_0^3-(3m-1)\omega_0^2+3(m+1)^2\omega_0-m^3-7m^2-3m+3\right]$$
$$+2k_0^2(\omega_0-m-1)^2-4\left[m\omega_0^2-2(m+1)^2\omega_0+(m+1)(m^2+3m-2)\right]\frac{k_0K_m}{K_{m+1}}$$
$$-2(\omega_0-m+1)(\omega_0-m-3)\frac{k_0^2K_m^2}{K_{m+1}^2}, \tag{C 14}$$

$$g^{(1)}=-\left(m-\frac{k_0K_{m+1}}{K_m}\right)\left[m(\omega_0-m-1)+\frac{k_0K_{m+1}}{K_m}\right], \tag{C 15}$$

$$g^{(2)}=\left(m+1+\frac{k_0K_m}{K_{m+1}}\right)\left[(m+1)(\omega_0-m)+\frac{k_0K_m}{K_{m+1}}\right], \tag{C 16}$$

$$h=(\omega_0-m)(\omega_0-m-1)\left\{(m+1)(\omega_0-m+2)\frac{k_0K_{m+1}}{K_m}+m(\omega_0-m-3)\frac{k_0K_m}{K_{m+1}}\right.$$
$$\left.-2m(m+1)\right\}A_1+2k_0^2A_5+(2\omega_0-2m-1)k_0^3\left\{\left[A_1-6\left(3\omega_0^2-3\omega_0-3m^2+1\right)\right]\right.$$
$$\left.\times\frac{K_{m+1}}{K_m}-\left[A_1-6\left(3\omega_0^2+3\omega_0-3m^2-6m-2\right)\right]\frac{K_m}{K_{m+1}}\right\}, \tag{C 17}$$

where

$$A_5=9\omega_0^6-36(2m+1)\omega_0^5+(225m^2+225m+46)\omega_0^4-9(2m+1)(20m^2+20m-3)\omega_0^3$$
$$+(315m^4+630m^3+126m^2-189m-38)\omega_0^2-m(m+1)(2m+1)$$
$$\times(72m^2+72m-115)\omega_0+27m^6+81m^5+12m^4-111m^3-71m^2-2m+4. \tag{C 18}$$

The coefficients associated with the viscous effect are

$$\Delta^{(1)}=-m\left[\omega_0^2-2(m+1)\omega_0+m^2+2m+4+\frac{16m(\omega_0-m-1)}{(\omega_0-m)^2}\right]+4k_0^2$$
$$+\left[\omega_0^2-2m\omega_0+m^2+8m+4+\frac{16m(\omega_0-m-2)}{(\omega_0-m)^2}\right]\frac{k_0K_{m+1}}{K_m}$$
$$-\frac{4(\omega_0-m+2)(\omega_0-m-2)}{(\omega_0-m)^2}\frac{k_0^2K_{m+1}^2}{K_m^2}, \tag{C 19}$$

$$\Delta^{(2)} = (m+1)\left[\omega_0^2 - 2m\omega_0 + m^2 + 3 + \frac{16(m+1)(\omega_0 - m)}{(\omega_0 - m - 1)^2}\right] + 4k_0^2$$
$$+ \left[\omega_0^2 - 2(m+1)\omega_0 + m^2 - 6m - 3 + \frac{16(m+1)(\omega_0 - m + 1)}{(\omega_0 - m - 1)^2}\right]\frac{k_0 K_m}{K_{m+1}}$$
$$- \frac{4(\omega_0 - m + 1)(\omega_0 - m - 3)}{(\omega_0 - m - 1)^2}\frac{k_0^2 K_m^2}{K_{m+1}^2}. \tag{C 20}$$

Appendix D. Short-wavelength asymptotics of the dispersion relation

We shall carry out asymptotic expansions of (k_0, ω_0) for intersection points between dispersion curves of the m and the $m+1$ Kelvin waves, valid at large k_0 in § D.1, and valid at large m with $\eta_1 \sim \eta_2 \sim m$ in § D.2. A similar analysis was made in the context of the MSTW instability by Fukumoto (2003) (see also Eloy & Le Dizès 2001).

D.1. *Large k_0 with m fixed*

Anticipating that $\omega_0 \to m + 1/2$ as $k_0 \to \infty$, we pose $\omega_0 = m + 1/2 + \sum_{i=1} c_i k_0^{-i}$, an expansion in powers of $1/k_0$, and determine the constants c_1 and c_2.

For the m wave, (B 4) is expanded as

$$\eta_1 = \sqrt{15}k_0 - \frac{32c_1}{\sqrt{15}} - \frac{32}{\sqrt{15}k_0}\left(c_2 - \frac{29c_1^2}{15}\right) + O\left(k_0^{-3}\right). \tag{D 1}$$

Using the large-wavenumber asymptotic expansions

$$\left.\begin{aligned} \frac{K_{m+1}(k_0)}{K_m(k_0)} &= 1 + \frac{2m+1}{2k_0} + \frac{4m^2-1}{8k_0^2} + O\left(k_0^{-3}\right), \\ J_m(\eta_1) &= \left\{1 - \frac{(4m^2-1)(4m^2-9)}{128\eta_1^2}\right\}\cos\left(\eta_1 - \frac{2m+1}{4}\pi\right) \\ &\quad - \frac{4m^2-1}{8\eta_1^2}\sin\left(\eta_1 - \frac{2m+1}{4}\pi\right) + O\left(\eta_1^{-3}\right), \end{aligned}\right\} \tag{D 2}$$

and the similar one for $J_{m+1}(\eta_1)$ (Abramowitz & Stegun 1965), (B 6) is expanded, for a cograde radial mode ($\omega_0 > m$), as

$$k_0 - \frac{32c_1}{15} - \frac{32}{15k_0}\left(c_2 - \frac{29c_1^2}{15}\right) = \frac{\pi}{\sqrt{15}}\left\{l_1 + \frac{2m-1}{4} + \frac{1}{\pi}\arctan\left(\frac{1}{\sqrt{15}}\right)\right\}$$
$$- \frac{2}{15k_0}\left(c_1 - \frac{4m^2+2m+3}{16}\right) + O\left(k_0^{-2}\right), \tag{D 3}$$

where l_1 is a large integer that labels branches of the m wave, with $l_1 = 1$ corresponding to the first cograde radial mode. Proceeding similarly to the $m+1$ wave, the asymptotic expansion of (B 7) is deduced, for $\omega_0 < m+1$, as

$$k_0 + \frac{32c_1}{15} + \frac{32}{15k_0}\left(c_2 + \frac{29c_1^2}{15}\right) = \frac{\pi}{\sqrt{15}}\left\{l_2 + \frac{2m-3}{4} + \frac{1}{\pi}\arctan\left(\frac{1}{\sqrt{15}}\right)\right\}$$
$$- \frac{2}{15k_0}\left(c_1 + \frac{4m^2+6m+5}{16}\right) + O\left(k_0^{-2}\right), \tag{D 4}$$

where l_2 is a large labelling integer with $l_2 = 1$ corresponding to the isolated mode. The first retrograde radial mode is labelled $l_2 = 2$.

The constants c_1 and c_2 that fulfil (D 3) and (D 4) simultaneously furnish the desired asymptotic expression for ω_0 for an intersection point as

$$\omega_0 = m + \frac{1}{2} + \frac{\sqrt{15}\pi\Delta' l}{128k_0} - \frac{1}{128k_0^2}\left\{m + \frac{1}{2} + \frac{\sqrt{15}\pi\Delta' l}{16}\right\} + O\left(k_0^{-3}\right). \tag{D 5}$$

Here we have introduced

$$\Delta l = l_2 - l_1, \quad \Delta' l = 2\Delta l - 1. \tag{D 6}$$

The intersection wavenumber is obtained by solving (D 3)

$$k_0 = \frac{1}{\sqrt{15}}\left\{\frac{\pi(l_1 + l_2 + m - 1)}{2} + \arctan\left(\frac{1}{\sqrt{15}}\right)\right\} - \frac{1}{30k_0}\left\{m^2 + m + 1 + \frac{29\pi^2(\Delta' l)^2}{256}\right\} + O\left(k_0^{-2}\right), \tag{D 7}$$

iteratively for large integers l_1 and l_2.

D.2. *Large k_0 and m with $\eta_1 \sim \eta_2 \sim m$*

The increasing power of m with order of expansion in the coefficients of (D 5) and (D 7) leads to breakdown of the above expansions. A separate treatment is required for large values of m.

The short-wave asymptotics for the m wave was derived by Fukumoto (2003), and we repeat it for convenience. We eliminate ω_0, in terms of the radial wavenumber η_1, from the dispersion relation (B 6) for the m wave, leaving

$$\left\{\frac{\eta_1}{k_0}\frac{K_m'(k_0)}{K_m(k_0)} - \frac{m}{\eta_1}\sqrt{1 + \left(\frac{\eta_1}{k_0}\right)^2}\right\} J_m(\eta_1) + J_m'(\eta_1) = 0, \tag{D 8}$$

where a prime stands for differentiation with respect to the argument. The dominant mode is expected to emerge in the regime of $\eta_1 \sim m$. The asymptotics of the Bessel functions, valid for this regime, are

$$J_m\left(m + \xi m^{1/3}\right) = 2^{1/3}\left(\frac{1}{m^{1/3}} - \frac{\xi}{5m}\right)\mathrm{Ai}\left(-2^{1/3}\xi\right) + \frac{3 \times 2^{2/3}\xi^2}{10m}\mathrm{Ai}'\left(-2^{1/3}\xi\right) + O\left(m^{-5/3}\right), \tag{D 9}$$

$$\frac{K_m'(k_0)}{K_m(k_0)} = -\frac{(1+\kappa^2)^{1/2}}{\kappa}\left\{1 + \frac{\kappa^2}{2m(1+\kappa^2)^{3/2}}\right\} + O(m^{-2}), \tag{D 10}$$

where Ai is the Airy function, ξ is some constant of order unity and

$$\kappa = k_0/m \tag{D 11}$$

is assumed to be finite. Then η_1 is obtained from (D 8) in the form of a power series in $m^{-1/3}$ as

$$\eta_1 = m - \frac{a_1}{2^{1/3}}m^{1/3} + \frac{\kappa^2}{(\kappa+1)(\kappa^2+1)^{1/2}} + \frac{3a_1^2}{10 \times 2^{2/3}m^{1/3}} - \frac{a_1\kappa^2(\kappa^4 - 3\kappa^2 - 3\kappa - 3)}{3 \times 2^{1/3}m^{2/3}(\kappa+1)^3(\kappa^2+1)^{3/2}} + O(m^{-1}), \tag{D 12}$$

where $a_1 (< 0)$ is a zero of the Airy function Ai.

Repetition of this procedure for the dispersion relation of the $m+2$ wave

$$\left\{\frac{\eta_2}{k_0}\frac{K'_{m+1}(k_0)}{K_{m+1}(k_0)}+\frac{m+1}{\eta_2}\sqrt{1+\left(\frac{\eta_2}{k_0}\right)^2}\right\}J_{m+1}(\eta_2)+J'_{m+1}(\eta_2)=0, \tag{D 13}$$

yields

$$\eta_2 = m-\frac{a_2}{2^{1/3}}m^{1/3}+1-\frac{\kappa^2}{(\kappa-1)(\kappa^2+1)^{1/2}}+\frac{3a_2^2}{10\times 2^{2/3}m^{1/3}} + \frac{a_2}{3\times 2^{1/3}m^{2/3}}\left\{\frac{\kappa^2(\kappa^4-3\kappa^2+3\kappa-3)}{(\kappa-1)^3(\kappa^2+1)^{3/2}}-1\right\}+O(m^{-1}), \tag{D 14}$$

where $a_2(<0)$ is a zero of Ai.

Being coupled with the definition (B 4) and (B 8) for η_1 and η_2 respectively, the crossing point (ω_0, k_0) of dispersion curves of the m, $m+1$ waves is obtained as the simultaneous solution of (D 12) and (D 14) in the form of power series in $m^{-1/3}$ as

$$k_0 = \frac{m}{\sqrt{15}}-\frac{a_1+a_2}{2^{4/3}\sqrt{15}}m^{1/3}+\frac{1}{56}+\frac{1}{2\sqrt{15}}-\frac{49(a_1^2+a_2^2)-290a_1a_2}{640\times 2^{1/3}\sqrt{15}m^{1/3}}+\frac{1}{87808\times 2^{1/3}} \times\left[\frac{2}{3\sqrt{15}}(-64429a_1+42477a_2)-725(a_1+a_2)\right]\frac{1}{m^{2/3}}+O(m^{-1}), \tag{D 15}$$

$$\omega_0 = m+\frac{1}{2}+\frac{15(a_1-a_2)}{64\times 2^{1/3}m^{2/3}}+\frac{435}{1792m}+\frac{3(a_1^2-a_2^2)}{64\times 2^{2/3}m^{4/3}}+\frac{5}{1404928\times 2^{1/3}} \times[2535\sqrt{15}(-a_1+a_2)+169a_1+44073a_2]\frac{1}{m^{5/3}}+O(m^{-2}). \tag{D 16}$$

REFERENCES

Abramowitz, M. & Stegun, I. A. 1965 *Handbook of Mathematical Functions*. Dover.

Arms, R. J. & Hama, F. R. 1965 Localized-induction concept on a curved vortex and motion of an elliptic vortex ring. *Phys. Fluids* **8**, 553–559.

Bayly, B. J. 1986 Three-dimensional instability of elliptical flow. *Phys. Rev. Lett.* **57**, 2160–2163.

Cairns, R. A. 1979 The role of negative energy waves in some instabilities of parallel flows. *J. Fluid Mech.* **92**, 1–14.

Crow, S. C. 1970 Stability theory for a pair of trailing vortices. *AIAA J.* **8**, 2172–2179.

Dellnitz, M., Melbourne, I. & Marsden, J. E. 1992 Generic bifurcation of Hamiltonian vector fields with symmetry. *Nonlinearity* **5**, 979–996.

Dyson, F. W. 1893 The potential of an anchor ring. – part II. *Phil. Trans. R. Soc. Lond.* A **184**, 1041–1106.

Eloy, C. & Le Dizès, S. 1999 Three-dimensional instability of Burgers and Lamb-Oseen vortices in a strain field. *J. Fluid Mech.* **378**, 145–166.

Eloy, C. & Le Dizès, S. 2001 Stability of the Rankine vortex in a multipolar strain field. *Phys. Fluids* **13**, 660–676.

Fraenkel, L. E. 1970 On steady vortex rings of small cross-section in an ideal fluid. *Proc. R. Soc. Lond.* A **316**, 29–62.

Fraenkel, L. E. 1972 Examples of steady vortex rings of small cross-section in an ideal fluid. *J. Fluid Mech.* **51**, 119–135.

Fukumoto, Y. 2002 Higher-order asymptotic theory for the velocity field induced by an inviscid vortex ring. *Fluid Dyn. Res.* **30**, 67–95.

Fukumoto, Y. 2003 The three-dimensional instability of a strained vortex tube revisited. *J. Fluid Mech.* **493**, 287–318.

Fukumoto, Y. & Hattori, Y. 2002 Linear stability of a vortex ring revisited. In *Proc. IUTAM Symposium on Tubes, Sheets and Singularities in Fluid Dynamics* (ed. H. K. Moffatt & K. Bajer), pp. 37–48. Kluwer.

Fukumoto, Y. & Moffatt, H. K. 2000 Motion and expansion of a viscous vortex ring. Part 1. A higher-order asymptotic formula for the velocity. *J. Fluid Mech.* **417**, 1–45.

Gledzer, E. B., Dolzhansky, F. V., Obukhov, A. M. & Ponomarev, V. M. 1975 An experimental and theoretical study of the stability of motion of a liquid in an elliptical cylinder. *Izv. Atoms. Ocean. Phys.* **11**, 617–622.

Gledzer, E. B. & Ponomarev, V. M. 1992 Instability of bounded flows with elliptical streamlines. *J. Fluid Mech.* **240**, 1–30.

Guckenheimer, J. & Mahalov, A. 1992 Instability induced by symmetry reduction. *Phys. Rev. Lett.* **68**, 2257–2260.

Hattori, Y. & Fukumoto, Y. 2003 Short-wavelength stability analysis of thin vortex rings. *Phys. Fluids* **15**, 3151–3163.

Kerswell, R. R. 1993 The instability of precessing flow. *Geophys. Astrophys. Fluid Dyn.* **72**, 107–144.

Kerswell, R. R. 2002 Elliptical instability. *Annu. Rev. Fluid Mech.* **34**, 83–113.

Knobloch, E., Mahalov, A. & Marsden, J. E. 1994 Normal forms for three-dimensional parametric instabilities in ideal hydrodynamics. *Physica* D **73**, 49–81.

Kop'ev, V. F. & Chernyshev, S. A. 2000 Vortex ring oscillations, the development of turbulence in vortex rings and generation of sound. *Phys. Uspekhi* **43**, 663–690.

Kopiev, V. F. & Chernyshev, S. A. 1997 Vortex ring eigen-oscillations as a source of sound. *J. Fluid Mech.* **341**, 19–57.

Krasny, R., Lindsay, K. & Nitsche, M. 2002 Simulation of vortex sheet roll-up: chaos, azimuthal waves, ring merger. In *Proc. IUTAM Symposium on Tubes, Sheets and Singularities in Fluid Dynamics* (ed. H. K. Moffatt & K. Bajer), pp. 3–12. Kluwer.

Leweke, T. & Williamson, C. H. K. 1998 Cooperative elliptic instability of a vortex pair. *J. Fluid Mech.* **360**, 85–119.

Lifschitz, A. & Hameiri, E. 1991 Local stability conditions in fluid dynamics. *Phys. Fluids* A **3**, 2644–2651.

Lugomer, S. & Fukumoto, Y. 2005 Hierarchical instability of a vortex ring array in multipulse laser-matter interactions. *Fluid Dyn. Res.* (to appear).

MacKay, R. S. 1986 Stability of equilibria of Hamiltonian systems. In *Nonlinear Phenomena and Chaos* (ed. S. Sarkar), pp. 254–270. Adam Hilger, Bristol.

Mahalov, A. 1993 The instability of rotating fluid columns subjected to a weak external Coriolis force. *Phys. Fluids* A **5**, 891–900.

Marsden, J. E. 1992 *Lecture on Mechanics*. London Mathematical Society Lecture Notes Series vol. 174, Chap. 10. Cambridge University Press.

Mason, R. M. & Kerswell, R. R. 2002 Chaotic dynamics in a strained rotating flow: a precessing plane fluid layer. *J. Fluid Mech.* **471**, 71–106.

Maxworthy, T. 1972 The structure and stability of vortex rings. *J. Fluid Mech.* **51**, 15–32.

Maxworthy, T. 1977 Some experimental studies of vortex rings. *J. Fluid Mech.* **81**, 465–495.

Moore, D. W. & Saffman, P. G. 1975 The instability of a straight vortex filament in a strain field. *Proc. R. Soc. Lond.* A **346**, 413–425.

Naitoh, T., Fukuda, N., Gotoh, T., Yamada, H. & Nakajima, K. 2002 Experimental study of axial flow in a vortex ring. *Phys. Fluids* **14**, 143–149.

Norbury, J. 1973 A family of steady vortex rings. *J. Fluid Mech.* **57**, 417–431.

Saffman, P. G. 1978 The number of waves on unstable vortex rings. *J. Fluid Mech.* **84**, 625–639.

Saffman, P. G. 1992 *Vortex Dynamics*, Chap. 12. Cambridge University Press.

Shariff, K. & Leonard, A. 1992 Vortex rings. *Annu. Rev. Fluid Mech.* **24**, 235–279.

Shariff, K., Verzicco, R. & Orlandi, P. 1994 A numerical study of three-dimensional vortex ring instabilities: viscous corrections and early nonlinear stage. *J. Fluid Mech.* **279**, 351–375.

Tsai, C.-Y. & Widnall, S. E. 1976 The stability of short waves on a straight vortex filament in a weak externally imposed strain field. *J. Fluid Mech.* **73**, 721–733.

Waleffe, F. 1990 On the three-dimensional instability of strained vortices. *Phys. Fluids* A **2**, 76–80.

Weigand, A. & Gharib, M. 1997 On the evolution of laminar vortex rings. *Exps. Fluids* **22**, 447–457.

Widnall, S. E., Bliss, D. B. & Tsai, C.-Y. 1974 The instability of short waves on a vortex ring. *J. Fluid Mech.* **66**, 35–47.

Widnall, S. E. & Sullivan, J. P. 1973 On the stability of vortex rings. *Proc. R. Soc. Lond.* A **332**, 335–353.

Widnall, S. E. & Tsai, C.-Y. 1977 The instability of the thin vortex ring of constant vorticity. *Phil. Trans. R. Soc. Lond.* A **287**, 273–305 (referred to herein as WT77).